Technical Document 1635
August 1989

Effect of Marine Atmosphere on Performance of Electrooptical Systems

J. H. Richter
H. G. Hughes
M. R. Paulson

NAVAL OCEAN SYSTEMS CENTER

San Diego, California 92152-5000

E. G. SCHWEIZER, CAPT, USN
Commander

R. M. HILLYER
Technical Director

ADMINISTRATIVE INFORMATION

This work was performed from 30 September 1988 to 30 September 1989 for the Office of Navy Technology, Code 214.

Released by
H. V. Hitney, Head
Tropospheric Branch

Under authority of
J. H. Richter, Head
Ocean and Atmospheric
Sciences Division

SM

REPORT DOCUMENTATION PAGE

1a. REPORT SECURITY CLASSIFICATION UNCLASSIFIED	1b. RESTRICTIVE MARKINGS
2a. SECURITY CLASSIFICATION AUTHORITY	3. DISTRIBUTION/AVAILABILITY OF REPORT Approved for public release; distribution is unlimited.
2b. DECLASSIFICATION/DOWNGRADING SCHEDULE	
4. PERFORMING ORGANIZATION REPORT NUMBER(S) NOSC TD 1635	5. MONITORING ORGANIZATION REPORT NUMBER(S)
6a. NAME OF PERFORMING ORGANIZATION Naval Ocean Systems Center 6b. OFFICE SYMBOL (If applicable)	7a. NAME OF MONITORING ORGANIZATION
6c. ADDRESS (City, State and ZIP Code) San Diego, CA 92152-5000	7b. ADDRESS (City, State and ZIP Code)
8a. NAME OF FUNDING/SPONSORING ORGANIZATION Office of Navy Technology 8b. OFFICE SYMBOL (If applicable) Code 214	9. PROCUREMENT INSTRUMENT IDENTIFICATION NUMBER
8c. ADDRESS (City, State and ZIP Code) Arlington, VA	10. SOURCE OF FUNDING NUMBERS PROGRAM ELEMENT NO.: 62435N PROJECT NO.: RM35G80 TASK NO.: N01A AGENCY ACCESSION NO.: 540SXB3

11. TITLE (Include Security Classification)
EFFECT OF MARINE ATMOSPHERE ON PERFORMANCE OF ELECTROOPTICAL SYSTEMS

12. PERSONAL AUTHOR(S)
J. H. Richter, H. G. Hughes, M. R. Paulson

13a. TYPE OF REPORT	13b. TIME COVERED	14. DATE OF REPORT (Year, Month, Day)	15. PAGE COUNT
Final	FROM 30 Sep 88 TO 30 Sep 89	August 1989	45

16. SUPPLEMENTARY NOTATION

17. COSATI CODES			18. SUBJECT TERMS (Continue on reverse if necessary and identify by block number)
FIELD	GROUP	SUB-GROUP	optical propagation IR radiance aerosols

19. ABSTRACT (Continue on reverse if necessary and identify by block number)

This report reviews the exploratory development effort in the US Navy to provide an atmospheric effects assessment capability for existing and planned electrooptical (EO) systems. For many EO system applications, it is necessary to have an accurate knowledge of marine background radiances and to consider the effects of the intervening atmosphere. Accordingly, a capability was developed to estimate the apparent sea surface radiance for different sea states and meteorological conditions. Also, an empirical relationship was developed which directly relates apparent mean sea temperature to calculated mean sky temperature.

A careful investigation was conducted of lidar (light detection and ranging) techniques. It was concluded that single-ended, single-frequency lidars cannot be used to infer slant-path extinction with an accuracy necessary to make meaningful performance assessments. Other lidar configurations may find limited application in model validation and research efforts. No technique has emerged yet which could be considered ready for shipboard implementation.

A shipboard real-time performance assessment system was developed and named PREOS (Performance and Range for EO Systems). PREOS has been incorporated into the Navy's Tactical Environmental Support System (TESS). The present versions of PREOS is a first step in accomplishing the complex task or real-time systems performance assessment. Improved target and background models are under development and will be incorporated into TESS when tested and validated.

20. DISTRIBUTION/AVAILABILITY OF ABSTRACT	21. ABSTRACT SECURITY CLASSIFICATION	
☐ UNCLASSIFIED/UNLIMITED ☒ SAME AS RPT ☐ DTIC USERS	UNCLASSIFIED	
22a. NAME OF RESPONSIBLE PERSON J. H. Richter	22b. TELEPHONE (Include Area Code) (619) 553-3053	22c. OFFICE SYMBOL Code 54

DD FORM 1473, 84 JAN

83 APR EDITION MAY BE USED UNTIL EXHAUSTED
ALL OTHER EDITIONS ARE OBSOLETE

CONTENTS

INTRODUCTION

The US Navy currently uses or is planning to use a number of electrooptical (EO) systems. For example, forward-looking infrared (FLIR) thermal imaging systems are currently installed on many aircraft as an integral part of their weapon systems. Infrared search and track (IRST) systems are currently in a research and development stage. Heat-seeking or laser-guided weapons have been used for a long time and new systems are under development. To optimize the performance of these EO systems in tactical situations, a way to assess their performance is needed. For surveillance systems, this means a way to predict the system's ability to detect and correctly identify a target of interest; for weapon systems, a way to predict the system's ability to track and destroy the target.

An assessment of surveillance and tracking equipment naturally requires a knowledge of the limitations and capabilities of the operator and sensor hardware, but it also requires a knowledge of the thermal characteristics of the target and its natural background, and the transmissivity between the target and sensor. These latter parameters are required as inputs to computer algorithms which determine the ranges at which the equivalent blackbody temperature difference between the target at zero range and its background is degraded by the atmospheric transmittance to the minimum detectable or resolvable temperatures of the sensor.

Both target and background infrared signatures are controlled by the intervening atmosphere. For a surface ship, heating from the sun and internal sources, and cooling by the ambient winds and ship's motion (as well as solar insulation effects) cause the ship's temperature to vary. The apparent temperature difference between the ship and its background, as viewed by the sensor, will then depend upon the infrared transmittance and emission along the propagation path. To be of practical use in tactical situations, airborne FLIR systems must be able to detect and identify surface targets at ranges of several tens of kilometers. This requirement limits the depression viewing angles to within a few degrees of the horizontal. As an example, the range to a target as viewed from an altitude of 1 km with a 1-degree depression angle is 80 km. Depressing the viewing angle to 3 degrees places the target only 20 km away. For larger viewing angles, the infrared radiance of the sea surface is the primary contributor to the background scene. Closer to the horizon, however, the sky radiance reflections and emissions by the intervening atmosphere must be taken into account. While a smooth sea is a poor emitter of infrared radiation at the small viewing angles, emissions from the individual wave facets of a wind-ruffled sea contribute to the background scene.

The development of suitable target and background models to be used in computer algorithms of system performance presents a formidable task and is needed by both users and designers of EO systems. In 1978, the Under Secretary of Defense for Research and Engineering formulated goals to be followed by the three services to address the primary factors (e.g., aerosol extinction, gaseous absorption, refraction, and turbulence) affecting the transmission and emission characteristics of the atmosphere which determine system performance. Basically, these goals (as updated in 1982) are

- Accurately model propagation environments of naturally occurring and man-made aerosols and gases, including the effects of turbulence and multiple scattering. Relate the particulate constituents to measurable and predictable meteorological parameters.
- Develop atmospheric sensor systems for model validation, test, and operational support. Special emphasis should be given to studies of the applicability of sensing by light detecting and ranging (lidar).

- Relate atmospheric effects to the performance of military systems, in operational as well as in research and development activities, to include the development of tactical decision aids. This includes the consideration of transmission, background, and target factors which are based on climatologies or real-time environmental inputs.

Since their inception, considerable progress has been made toward meeting these goals. The effects of gaseous absorptions on radiance and transmittance have been adequately addressed in the LOWTRAN 7 code developed at the Air Force Geophysical Laboratory (Kneizys et al., 1988). Since multiple scattering by aerosols has recently been included in LOWTRAN 7 and turbulence has been addressed in the Army's Electro-Optical Systems Atmospheric Effects Library (EOSEAL) (Miller and Ricklin, 1987), they will not be covered here. In the following sections, examples will be presented of advances made toward meeting each of the goals, with primary emphasis on the measurement and modeling of absorption and scattering by aerosols and their effects on radiance and transmittance, which determine system performance. It is the purpose of this document to summarize past accomplishments, discuss present deficiencies, and define future directions for the assessment of Navy EO system performance.

MARINE AEROSOL MODELING

Selectable aerosol size distribution models are now available in LOWTRAN 7 for calculating their scattering and absorption properties. Of primary interest here is the Navy Maritime Aerosol Model (NAM) (Gathman, 1983). This model was developed by using an extensive set of measurements made in the Eastern Pacific (San Nicolas Island) during 1978, 1979, and 1980. These measurements were of broadband (visible through the far infrared) atmospheric transmission and meteorological parameters, aerosol size distributions, and radon concentrations. This was a cooperative effort between Navy Laboratories (Naval Ocean Systems Center, Naval Research Laboratory, Naval Surface Warfare Center, and Naval Weapons Center), the Pacific Missile Test Center, and the Naval Postgraduate School. Shipboard measurements in the Atlantic Ocean (USNS *Hayes*, 1977; USNS *Lynch*, 1983) of aerosol size distributions and meteorological parameters were also included in the model's development.

Key to the development of NAM was the recognition of a trimodal structure in aerosol size distributions plotted from the aforementioned field experiments. This trimodal distribution was interpreted as a superposition of three aerosol distributions; the smallest due to continental aerosols, an intermediate size dependent on the average wind speed, and the largest governed by the instantaneous wind. Accordingly, a size distribution model (at radius r) is the sum of three log-normal distributions given by

$$n(r) = \sum_{i=1}^{3} A_i \exp\left[\left(\ln \frac{r}{fr_i} \right)^2 \right] \qquad (\mathrm{cm}^{-3} \cdot \mu\mathrm{m}^{-1}) \tag{1}$$

where

$$A_1 = 2000(AM)^2 \tag{2}$$

$$A_2 = 5.866(V - 2.2) \tag{3}$$

$$A_3 = 10^{(0.06V - 2.8)} \tag{4}$$

Component A_1 represents the contribution by continental aerosols. AM is an air mass parameter that is allowed to range between integer values of 1 for open ocean and 10 for coastal areas and is given by

$$AM = INT(Rn \quad 4) + 1 \tag{5}$$

where Rn is the measured atmospheric radon content expressed in pCi m^3. In the absence of radon measurements, the air mass factor can be related to the elapsed time, T (days), for the air mass to reach the point of observation:

$$AM = INT[9 \exp(\quad T \quad 4)] + 1 \tag{6}$$

Components A_1 and A_3 represent equilibrium sea spray particles generated by the surface wind speed averaged over 24 hours ($\bar{V}$, in m s) and the current surface wind speed (V, in m s), respectively. In Eq. 1, r_i, the modal radius for each component referenced to a relative humidity of 80% (r_1 = 0.03 μm, r_2 = 0.24 μm, and r_3 = 2.0 μm), is allowed to grow with relative humidity (RH) according to the Fitzgerald (1975) formula:

$$F = [(2 \quad RH \quad 100) \quad 6(1 \quad RH \quad 100)]^{1 \quad 3} \tag{7}$$

The contribution to the total extinction or absorption by each component can then be written as

$$\sigma_{e,a}(\lambda)_i = (SF)\left\{ C_i \int_r Q_{e,a}(\lambda,r,m) \exp\left[\quad \left(\ln \frac{r}{fr_i} \right)^2 \right] r^2 dr \right\} \tag{8}$$

where $C_i = (0.001\pi/f)A_i$. The factor f^{-1} in the expression for C_i ensures a constant total number of particles as the relative humidity increases. $Q_{e,a}(\lambda,r,m)$ is the cross-section for either the extinction or absorption normalized to the geometrical cross-section of the spherical particle, and m is the complex refractive index, which is allowed to change from that of dry sea salt as the particle deliquesces with increasing humidity. LOWTRAN 6 provides precalculated values in tabular form of the parameter $\sigma_{e,a}(\lambda_i) \quad C_i$ at discrete wavelengths for four relative humidities (50%, 85%, 90%, and 99%), from which the average extinction for a specific wavelength band and relative humidity can be readily determined by interpolation. When an observed surface visibility (VIS_o) is available as an input to the model, the amplitudes of the three components are adjusted by a scaling factor (SF) so that the calculated aerosol extinction coefficient, σ_c, at a wavelength of 0.55 μm, is the same as the observed extinction, σ_o, determined from the relationship

$$VIS_o = \frac{3.912}{\sigma_o + \sigma_r} \tag{9}$$

where σ_r is the Rayleigh contribution to extinction at 0.55 μm.

This model has undergone extensive evaluation of the accuracy with which it can predict infrared radiance and transmission. It should be noted that the current wind speed component, A_3, is different from the value published in LOWTRAN 6 (Kneizys et al., 1983), which was $A_3 = 0.01527(V \quad 2.2)$. This modification was found to be necessary in order to match published measurements of infrared (8 12 mm) sky radiances (Hughes, 1987). In that work, it was determined that for low wind speed, the measured and calculated radiances agreed within 2% at the optical horizon. However, during moderate wind

speed, the current wind speed component of the aerosol model had to be lowered by factors near 0.05 for the calculated and measured radiances to agree. When the model was used, the discrepancies between measured and calculated infrared radiances were found to be insensitive to the 24-hour averaged wind component (Fig. 1). Measurements by de Leeuw (1986) of large particle size distributions ($r > 5$ microns) provided another method of evaluating the current wind speed component. In that work, size distributions were measured with an impactor at different altitudes (0.2 to 11 meters) above the sea surface. In order for the size distributions calculated with the model using measured surface meteorological parameters to agree with the measured values, the current wind speed component had to be lowered by a factor near 0.07 (Fig. 2). Within the measurement accuracies of both the radiance and particle size comparisons, the reduction factors in the A_3 component were in reasonable agreement.

The accuracy to which the model can predict extinction coefficients has also been tested against the transmissometer and meteorological measurements at San Nicolas Island (Gathman and Ulfers, 1983). Good correlations were obtained between calculated and measured extinctions for near and midinfrared wavelengths. However, for the far infrared, the calculated extinctions were 20% to 40% greater than those measured by the transmissometer. While these correlations may have been influenced by the uncorrected A_3 component, they were shown to be sensitive to the selection of the air mass factor and to whether the visibility was used as an input.

The model was developed to be as representative as possible of different atmospheric conditions; however, it cannot be expected to exactly reproduce the optical properties in a given location at any specific time. Neither of the techniques for selecting the air mass factor (radon count or air trajectory analysis) is currently available for shipboard use. Also the visibilities inferred from point-scattering devices onboard ship are most apt to be contaminated by ship effluences. A method is needed for selecting the input parameters so that the model best represents a particular situation. A remote-sensing technique has recently been developed (Hughes and Jensen, 1988) whereby unique values of the air mass factor and visibility can be selected for different meteorological conditions. These values are inferred from LOWTRAN calculations which agree with both the surface measurements of 8-12-μm horizon radiances and visible atmospheric optical depths determined from satellite-detected upwelling solar radiances.

For this study, a Piper Navajo aircraft, equipped with Rosemount temperature and pressure probes and an EG&G dewpoint sensor, made vertical spirals over the ocean to obtain the profile of temperature, relative humidity, and pressure which are required inputs to the LOWTRAN 6 computer code for calculating the sky radiances. (A Barnes PRT-5 radiation thermometer was also onboard the aircraft to measure sea surface temperatures from low-level constant-altitude flights.) At the time the meteorological parameters were obtained on 29 September and 25 November 1987, measurements of infrared (8-12 μm) horizon radiances were also made with a calibrated thermal imaging system (AGA THERMOVISION, model 780) having a 2.95-degree field-of-view lens. The thermal video processor system (THERMOTEKNIX) available with the AGA system displays the thermal scene on a computer screen in a format consisting of 128 pixel lines (0.023 deg pixel line). The response of the system is determined by placing a blackbody of known temperature (± 0.1°C for temperatures <50°C) in front of the lens aperture. The digitized video signal transfer function of the system then allows the blackbody temperature to be reproduced to within ± 0.2°C.

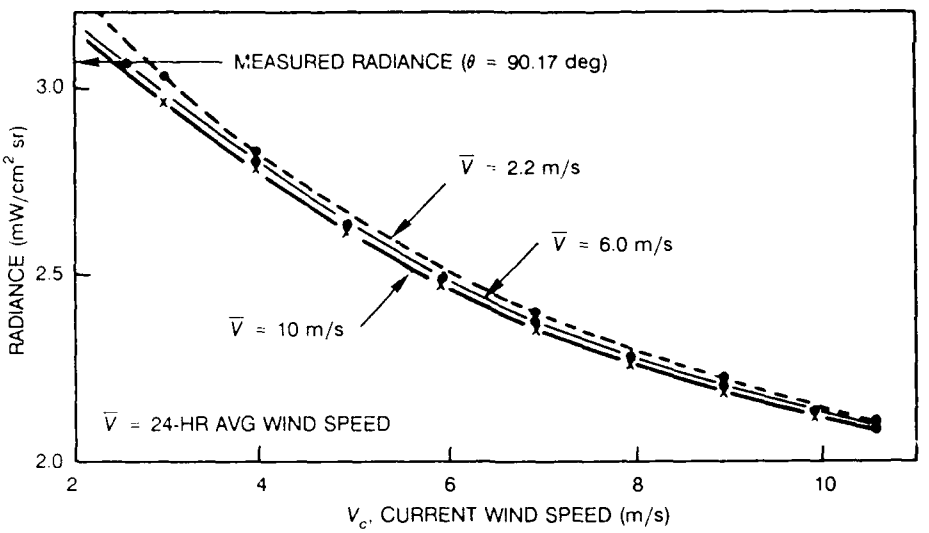

Figure 1. Sensitivity of the LOWTRAN 6 NAM to surface wind speed parameters.

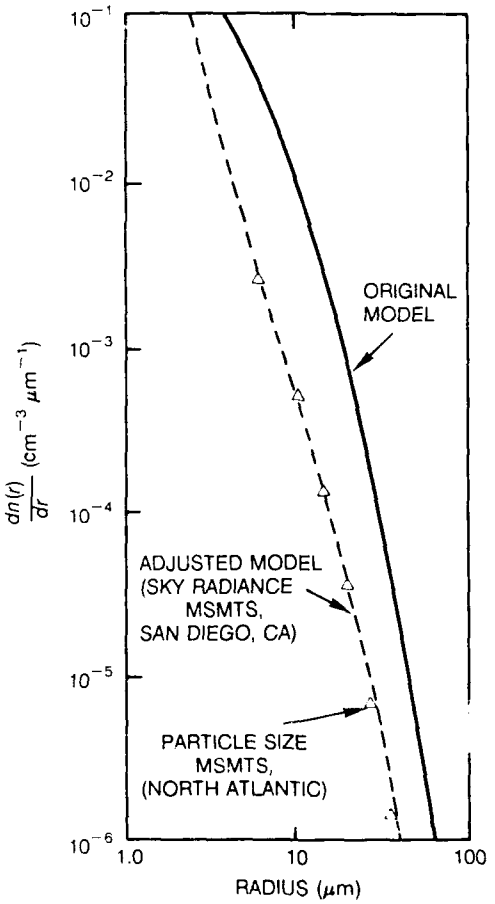

Figure 2. Comparisons of measured particle size distributions with distributions calculated with the original and adjusted LOWTRAN 6 NAM.

For these measurements, the scanner was located at an elevation of 33 meters on the Point Loma peninsula in San Diego and was directed due west over the ocean so that approximately half the field-of-view was above and half below the horizon. The data processing software of the AGA system also allows the the effective blackbody temperature of each pixel in the scene to be determined. On each of the days, the pixel corresponding to the maximum temperature in the thermogram (20.4°C on 29 September and 16.5°C on 25 November) was taken to coincide with the infrared horizon. From the current and 24-hour averaged wind speeds (V_c = 7.5 m s and $\bar{V}$ = 4.4 m s for 29 September, and V_c = 2.5 m s and $\bar{V}$ = 3.9 m s for 25 November) measured on shore at the AGA site, and the vertical profiles of meteorological parameters, LOWTRAN 6 calculations were made to agree with the maximum pixel radiance in the scene by using nonunique combinations of air mass factors and visibilities.

In these calculations, the meteorological profiles were divided into 33 layers, as allowed by LOWTRAN 6. The lower layers of the profiles are also divided into sublayers containing the same amount of absorbing and scattering material and the same temperature as the original layer. This artificial layering has been found necessary (Wollenweber, 1988a) to remove the anomalous dip (Hughes, 1987) which occurs when aerosols are included in the LOWTRAN 6 radiance calculations for zenith angles close to 90 degrees. Since the AGA scanner could not be accurately plumbed, the zenith angle of the infrared horizon (the pixel line corresponding to the maximum radiance) was taken to be one-half of a pixel line less than the angle at which the LOWTRAN calculations indicated the refracted ray path first struck the earth (Θ = 90.179 degrees on 29 September and 90.174 degrees on 25 November).

In Fig. 3, the solid lines represent the loci of points which allow the LOWTRAN calculations to match the measured horizon pixel radiances for different combinations of air mass factor and visibility. This feature of the calculations results from the visibility scaling factor of the size distribution remaining nearly constant for any appropriate combination of the two factors and from the relative insensitivity of the calculated extinction coefficients for the far infrared wavelengths to the air mass factor. At the time of the IR radiance measurements, upwelling solar radiances were detected by Channel 1 (0.58–0.65 μm) of the AVHRR on board the NOAA-9 satellite as it passed close to San Diego. These radiances, used to determine the total atmospheric optical depths (τ_a), were themselves determined by using the SAIC (Science Applications International Corp.) satellite radiance computer code, which makes use of a direct linear relationship between upwelling radiance and the total atmospheric optical depth (Griggs, 1975). Although the vertical structure of the meteorological parameters which control aerosol growth were different, the total optical depths for the two days were nearly identical. In a manner similar to the calculations of infrared radiance, calculations of total atmospheric optical depth were made to agree with the measurements made on both days. In calculating the optical depths, it was assumed that all the aerosols were confined to the mixed boundary layer as determined by the aircraft flights. The calculations of optical depths with different combinations of air mass factor and visibility are also shown in Fig. 3 as the dashed lines and are seen to be extremely sensitive to the air mass factor. The intersections of the solid and dashed lines then determine the best combinations of air mass factor and visibility to be used in the background calculations. The inset in the figure shows the good agreement between the inferred visibilities and those calculated by using aerosol size distributions measured at the lowest levels of the aircraft flights. These visibilities seem reasonable, since the Los Coronados Islands, located between 25 and 30 km off the coast of San Diego, were not visible to the naked eye on either day.

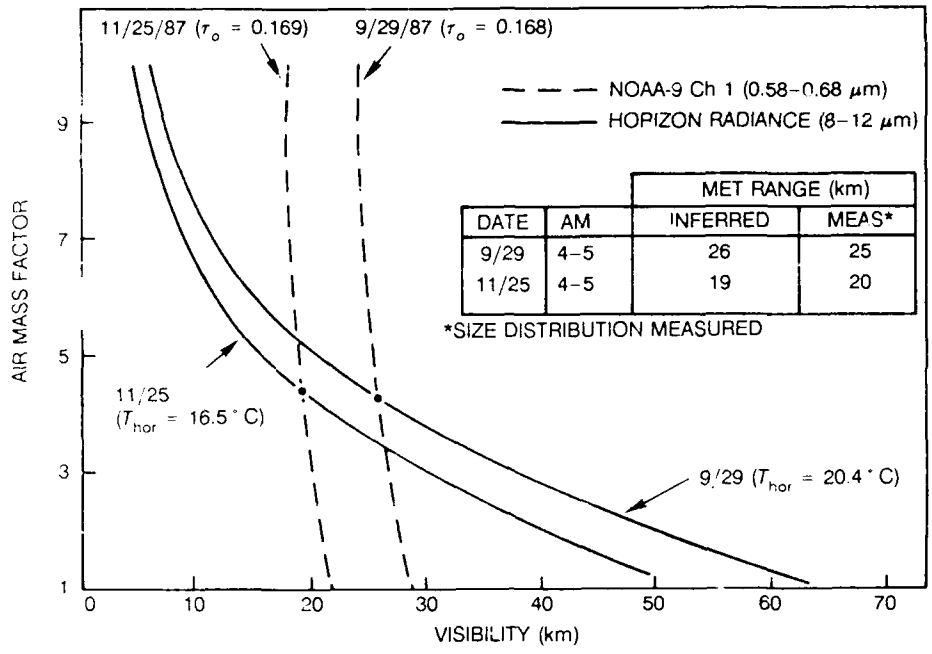

Figure 3. Loci of points of LOWTRAN 6 calculations with different combinations of air mass factors and visibilities which match measured values of IR horizon radiances (solid lines) and satellite-detected visible optical depths (dashed lines) for 29 September and 25 November 1987.

While NAM was initially developed by using surface measurements of aerosol size distributions and meteorological parameters, it is allowed to vary with altitude in LOWTRAN 6 according to relative humidity up to an altitude of 2 km, at which point the Tropospheric Model is introduced. A dynamic model using NAM as the surface kernel (the Navy Ocean Vertical Aerosol Model (NOVAM)) has recently been introduced (de Leeuw et al., 1989) to better account for the vertical variations in size distribution. It was developed through a cooperative effort between the Naval Research Laboratory, the Naval Postgraduate School, and the Naval Ocean Systems Center (Gathman, 1989). The Physics and Electronics Laboratory TNO, The Netherlands, recently joined in the evaluation and refinement effort (de Leeuw et al., 1989). The model is based on the physical processes affecting the production, mixing, deposition, and size of the aerosols within the marine atmosphere. Aerosols with similar origins are represented by separate log-normal size distributions. The net optical effect produced is the result of the superposition of all the aerosol groups. To determine the aerosol size distribution at any particular level, one of a set of mixing profile models is used. The selection process, indicated by the flow chart in Fig. 4, is determined by the meteorological input data available and the wavelength at which calculations are to be made. In addition to the general profiles of temperature and humidity as determined by radiosondes, the inputs required by NOVAM include the following set of surface observations:

- 24-hour averaged wind speed (m/s)
- Air mass factor (1 . . . 10)
- Cloud cover (tenths)
- Cloud type (1 . . . 10)

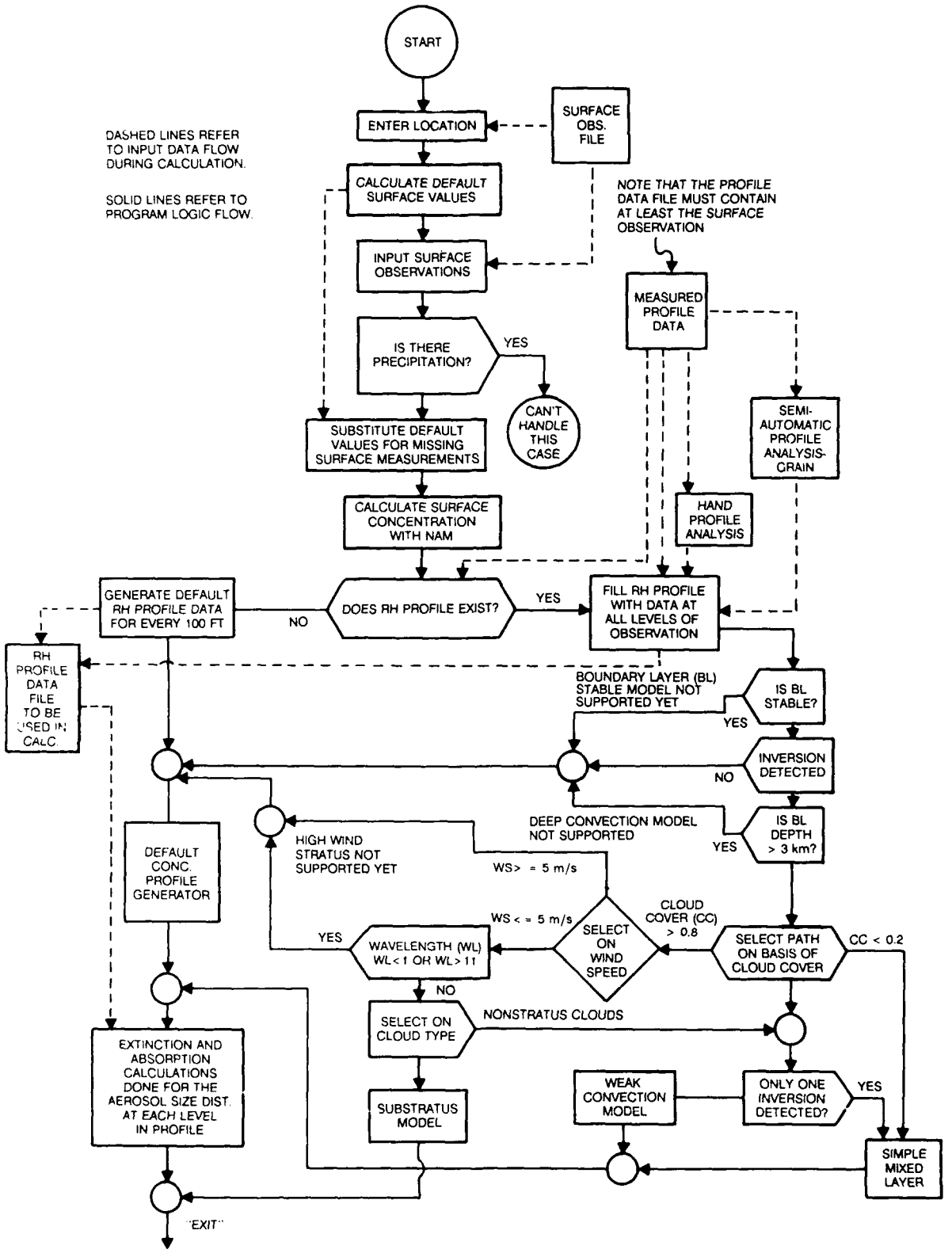

Figure 4. Flow chart for NOVAM.

- 10.6-μm extinction coefficient (km^{-1})
- Present weather in standard code (0...99)
- Height of lowest clouds (m)
- Zonal seasonal category (1...6)
- Sea surface temperature (°C)
- Air temperature (°C)
- Relative humidity (%)
- Optical visibility (km)
- Local wind speed (m s)

The product of NOVAM is primarily a file of the extinction and absorption coefficients at various levels in the marine atmosphere. While NAM has undergone numerous evaluations and considerable improvement through the use of transmission and sky radiance measurements, NOVAM has not yet received a critical evaluation. Such evaluation under well-defined environmental conditions is needed before it can be incorporated into LOWTRAN. Data for preliminary evaluations of NOVAM were obtained from measurements taken on the upwind side of San Nicolas Island on July 18, 1987, and have been presented elsewhere by de Leeuw et al. (1989). Figure 5 shows examples of extinction profiles at both visible and infrared wavelengths bands. The meteorological input data were obtained from a tethered balloon platform on which a nephelometer and a particle measuring system (PMS) particle spectrometer (Knollenberg) were located. Extinction at 0.55 μm is obtained directly from the nephelometer, whereas extinction at different wavelengths may be calculated from the size distributions obtained from the PMS. Figure 5a is the extinction profile for 0.55 μm measured with the nephelometer and calculated from the measured size distributions and from the NOVAM model. The data show considerable scatter in the measured extinctions with altitude. The NOVAM prediction is within the envelope of the scatter better than 75% of the time for this particular case.

Figure 5b shows the comparisons between the extinction coefficients for the 3–5-μm band calculated by using the model and the measured size distributions. A similar comparison for the 8–12-μm band calculated from the measured size distributions and the NOVAM prediction at 10.6 μm is shown in Fig. 5c. The present version of NOVAM underestimates the extinction in the infrared bands in the region above the mixed boundary layer. This may be a result of larger particles from the sea surface being mixed into the atmosphere above the apparent temperature inversion through the process of entrainment.

Additional evaluations of NOVAM have also been undertaken by using airborne data acquired in the Southern California area. The results indicate that predicted and measured extinction coefficient profiles have similar structure but may differ in absolute value. The agreements are strongly dependent upon the proper choices of air mass factors and the scaling to visibility. Default profiles of humidity and extinction do not in general represent the measured values.

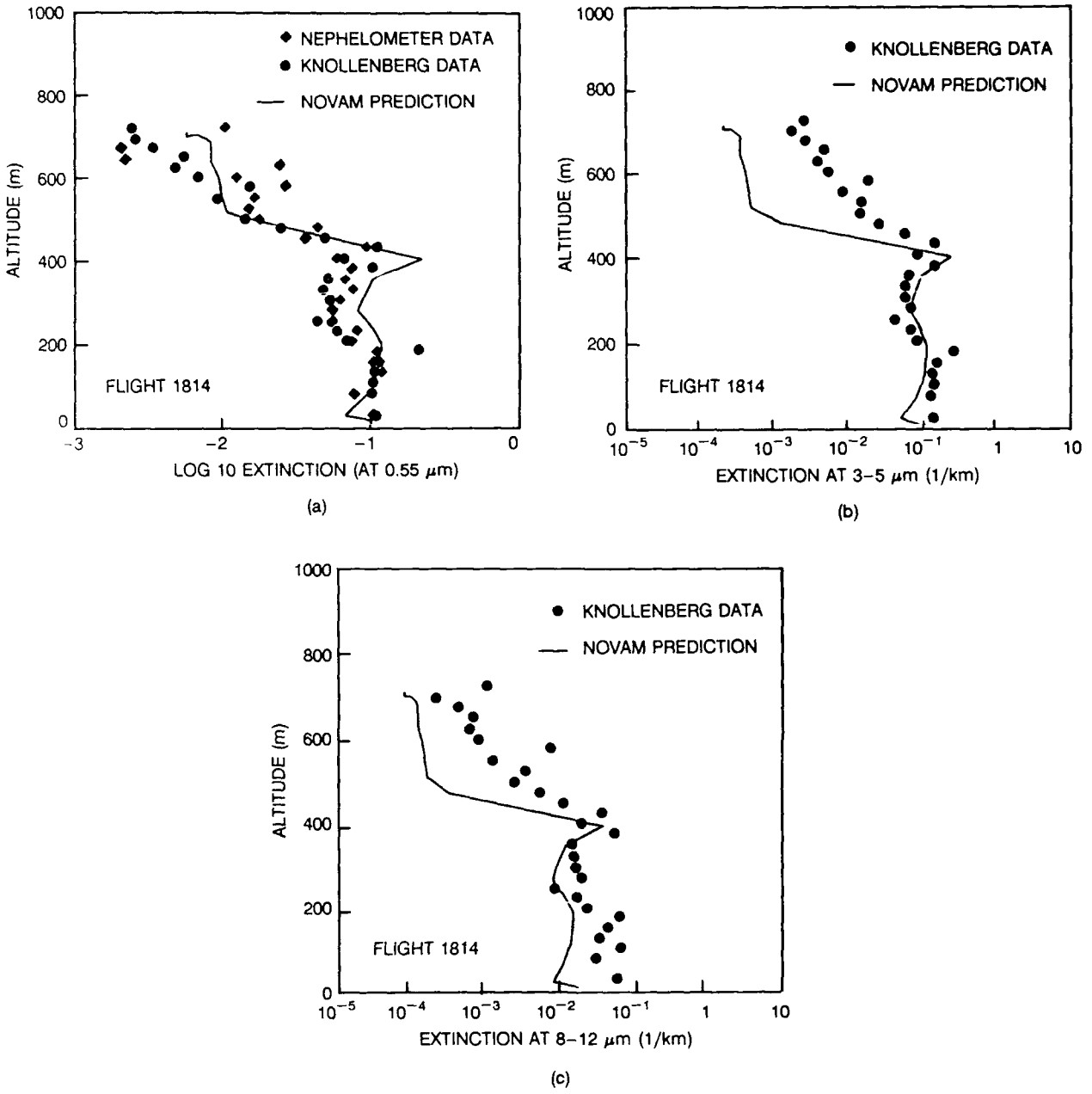

Figure 5. Comparison between extinction profiles predicted by NOVAM and experimental extinction profiles derived from nephelometer data or from particle size distributions using Mie theory (Knollenberg data). The measurements were made from a tethered balloon. (a) Comparison of the NOVAM prediction for a wavelength of 0.55 μm with a Mie calculated profile at 0.55 μm and the extinction profile derived from the nephelometer. (b) Comparison of the NOVAM prediction for the 3–5-μm band. (c) Comparison of the extinction profile as predicted by OVAM for 10.6 μm with the Mie calculated average extinction profile in the 8–12-μm band.

MARINE INFRARED BACKGROUNDS

As was demonstrated earlier, the LOWTRAN codes have proven to be a versatile tool in predicting atmospheric radiance above the horizon. They do not yet, however, include the capability of estimating the apparent radiance of the sea surface for different sea states and meteorological conditions. A model has recently been developed of the effective radiance of the sea surface as a function of the viewing zenith angle and sensor height (Wollenweber, 1988b) and has been incorporated into LOWTRAN 6 for processing on an HP-9020 computer. In addition to the path emissions, this version uses the Gaussian-distributed wave slope model of Cox and Munk (1954), which is based on surface wind speed and direction relative to the look angle. Currently limited to NAM, the model basically calculates the total contributions to radiance at the sensor from the emissions of the intervening atmosphere and the sky reflections and emissions from the wave slope surfaces.

Figures 6 and 7 show the comparisons of the measured and calculated infrared radiances for zenith angles within about 1 degree below the horizon for the air mass factors and visibilities for the 2 days in Fig. 3 (Hughes, 1989a). In both cases, the major contributor to the total radiance just below the horizon is the path emission $N(\Theta)_p$. While the reflected sky radiance $N(\Theta)_{rsk}$ and the surface emission $N(\Theta)_{ss}$ are small, their contribution to the total radiance $N(\Theta)_{tot}$ at this low level (33 m) of observation cannot be neglected. It is interesting to note only a small reversal of the relative magnitudes of the reflected sky

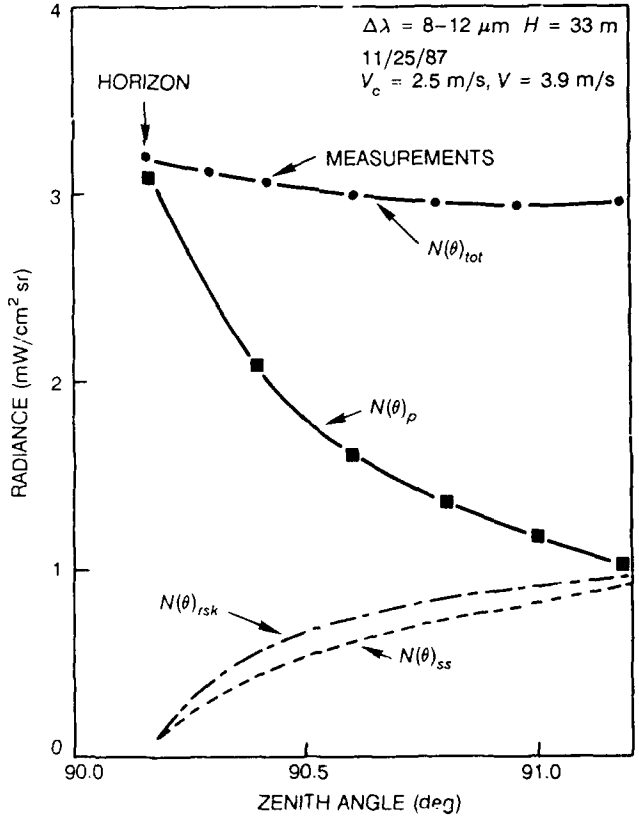

Figure 6. Comparison of the measured and calculated IR radiances for zenith angles about 1 degree below the horizon by using the air mass factors and visibilities determined for 25 November 1987.

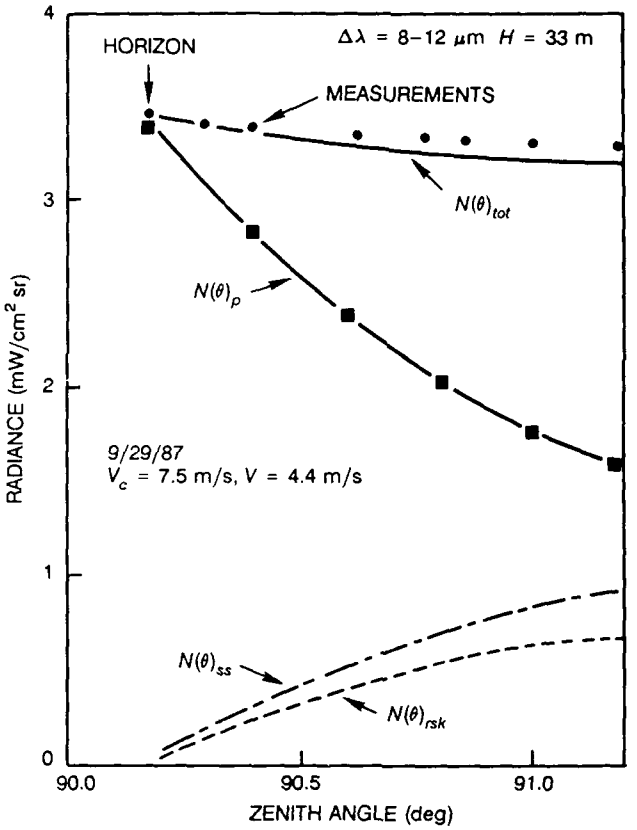

Figure 7. Comparison of the measured and calculated IR radiances for zenith angles about 1 degree below the horizon by using the air mass factors and visibilities determined for 29 September 1987.

radiances and surface emissions between the two sets of calculations, which demonstrates the small influence of the wave slopes for the moderate wind speeds on 29 September. Both the calculated and measured total radiances on both days are in good agreement, which places confidence in the model's usefulness in radiance calculations at other altitudes and zenith angles.

The selected aerosol models were used to calculate the contributions of the path, sea, and reflected sky radiances to the total background radiance as a function of altitude and zenith angle. In Fig. 8 and 9, examples are presented of calculations for both days with a sensor altitude of 1000 meters. For zenith angles less than about 95 degrees, the major contribution to the background is the path emission, with the reflected sky radiance being less than 10% of the total in both cases. In Fig. 10, the resulting apparent blackbody temperature of the sea versus zenith angle is compared for both days. Again, the higher apparent temperature for zenith angles near the horizon on 29 September results from the path emission from the warmer elevated layers. The rapid fall-off of path emission with increasing zenith angle (i.e., shorter slant paths to earth) is the cause of the decrease in

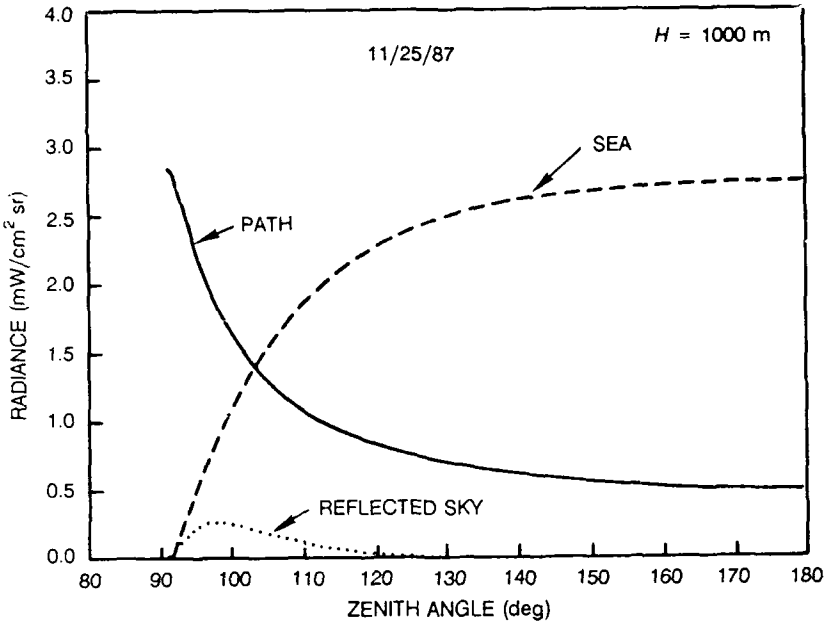

Figure 8. Calculations of contributions of the path, sea, and reflected sky radiances to the total background radiance as a function of zenith angle as viewed from an altitude of 1000 meters on 25 November 1987.

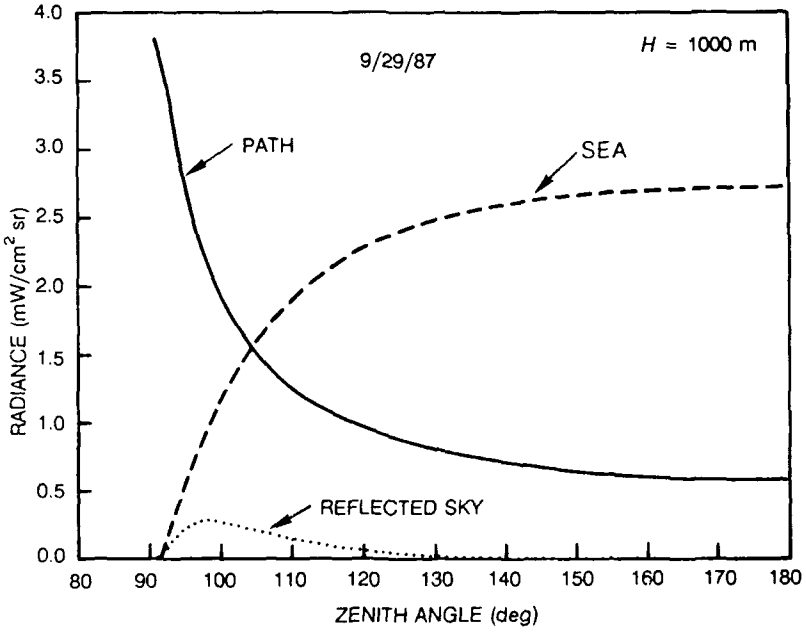

Figure 9. Calculations of contributions of the path, sea, and reflected sky radiances to the total background radiance as a function of zenith angle as viewed from an altitude of 1000 meters on 29 September 1987.

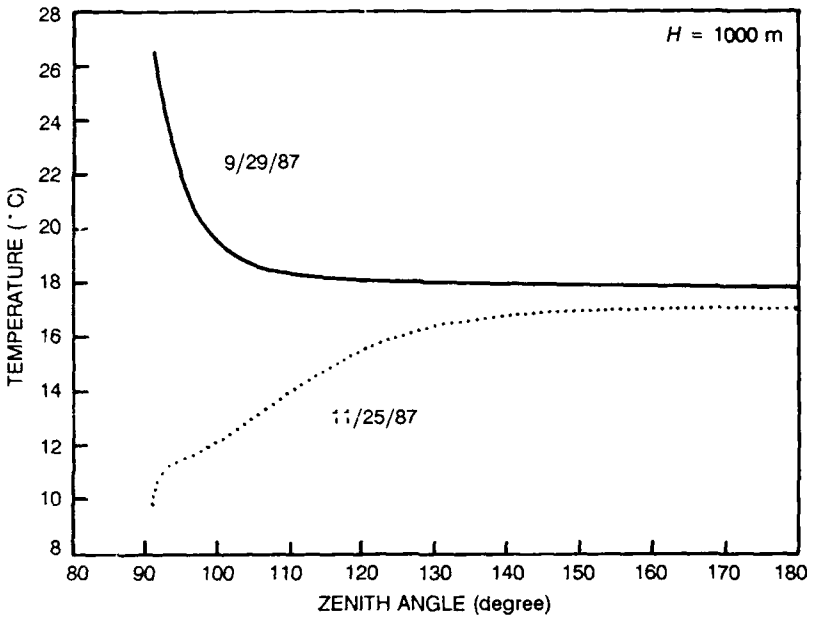

Figure 10. Calculations of the apparent blackbody temperature of the sea versus zenith angle as viewed from an altitude of 1000 meters on 29 September and 25 November 1987.

apparent temperature on this day. In contrast, the temperature increase on 25 November is the result of the increase in emission from the sea surface (which was warmer than the air) with increasing zenith angles. The relative contributions of the three components will of course change for other altitudes. As the nadir zenith angle is approached, the apparent temperatures at this altitude do not reach the measured sea surface temperatures (T_{ss} = 15.2°C on 29 September and T_{ss} = 17.6°C on 25 November) because of the path emission contributions at this altitude.

In a practical sense, the sea radiance model needs to be improved to reduce computer running time. In its present form, approximately 3 minutes of computational time on the HP-9020 is required to calculate the sea radiance at one zenith angle of viewing as compared to approximately 5 seconds for the sky radiance. Approximately 36 minutes of computer time is required to calculate the mean sea temperature within 1 degree of the horizon. The major contributor to the computational time is the large number of sky radiance reflections and surface emission calculations that must be made to account for the radiance from all the wave facets. Computational time could be saved if the surface emissivity and reflectivity calculations were made at a single representative wavelength instead of having to average over a wavelength band for each wave slope. Another way to reduce the computational time is to develop an empirical relationship to directly relate the apparent mean sea temperature to the calculated mean sky temperature.

To investigate this possibility, the THERMOTEKNIX system was used to determine the mean equivalent blackbody temperatures corresponding to an area 1 degree above and 1 degree below the horizon in thermograms taken during different surface wind speed conditions (Hughes, 1989b). For this study, 18 thermograms recorded during different meteorological and wind speed conditions in 1987 and 1988 were used to compare the mean sky and sea temperatures. In 12 of the cases, the actual sea surface temperature measured by the aircraft radiation thermometer was available. For the full data set, the mean temperatures were well correlated (coefficient of correlation, $r = 0.92$), as shown in Fig. 11, with the sea temperatures being less than the sky temperatures, as indicated by the dashed line for one-to-one correspondence. The mean temperatures differed the most during low wind speed conditions. These differences were found to decrease with increasing wind. Inherent in the observations are the actual sea surface temperatures and wind speeds. If these parameters are included in a multiple regression analysis for three independent variables, the following relationship is obtained for the mean sea surface temperature, $\bar{T}_m$(sea), in terms of the mean sky temperature, $\bar{T}_m$(sky), the current wind speed (V_c), and the actual sea surface temperature (T_{ss}):

$$\bar{T}_m(\text{sea}) = 1.09\ \bar{T}_m(\text{sky}) + 0.37\ V_c + 0.24\ T_{ss} \quad 10.5 \tag{10}$$

The correlation coefficient for the multiple regression analysis is 0.97. In this case, only 12 samples were used in the analysis (as compared to 18 samples in the linear regression analysis shown in Fig. 11), which indicates a definite improvement in the correlation when the actual sea surface temperatures and wind speeds are included.

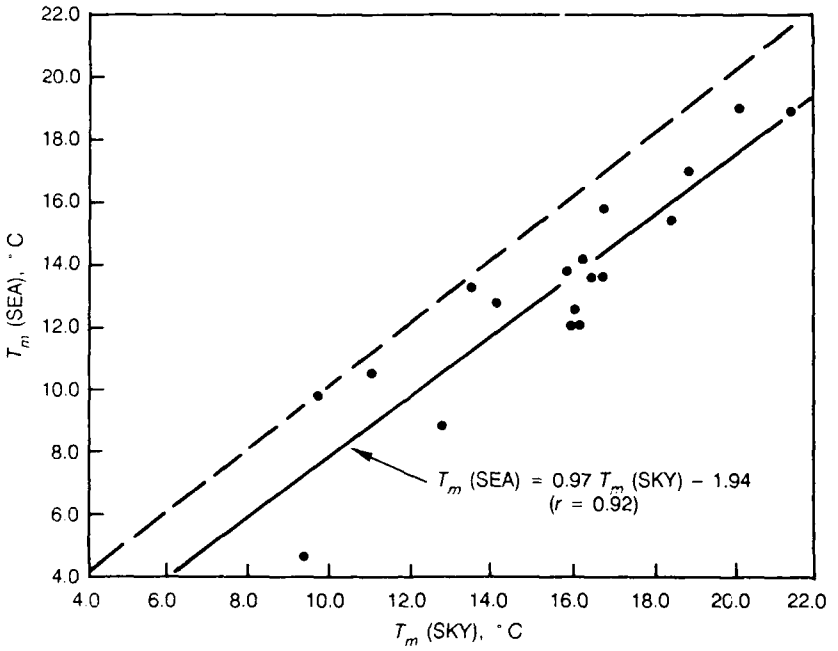

Figure 11. Regression analysis comparison of the measured mean sky temperatures, $\bar{T}_m$ (sky), and mean sea temperatures, $\bar{T}_m$ (sea). The dashed line corresponds to a one-to-one correspondence between the two parameters.

Earlier work (Hughes and Jensen, 1988) has demonstrated that the sky radiances measured at individual pixel lines within about 1 degree of the horizon can be modeled very closely by using the modified LOWTRAN 6 code. Based on this, the replacement of $\bar{T}_m(\text{sky})$ by a calculated value of the mean sky temperature, $\bar{T}_c(\text{sky})$, would appear justified. This would allow the mean sea temperature to be directly determined from Eq. 10 and measured profiles of meteorological parameters. Additional data are needed to verify that such a relationship for predicting the mean apparent temperature of the sea is meaningful for other meteorological conditions, sea states, and altitudes of observation. Such a relationship would be a valuable inclusion into a system designer's handbook as a tool for predicting infrared sea backgrounds in locales where only meteorological data are available.

AEROSOL SENSING WITH LIDARS

Measurements of slant-path visibilities are required as inputs to the LOWTRAN codes for scaling the selected size distributions with altitude. Lidar systems, which measure the radiation backscattered to a receiver by aerosols at different ranges within the beam of a laser pulse, have received considerable attention in recent years for this purpose. The technique of inverting a single-ended lidar return to obtain range-dependent atmospheric extinction coefficients requires an assumption concerning the relationship between the volumetric backscatter and extinction coefficients. Where the integration is performed in the forward direction (i.e., away from the receiver), the extinction coefficient $\sigma(r_o)$ out to the range where the transmitter and receiver field-of-view overlap, r_o, must be known. If the integration is performed in the reverse direction (toward the receiver), the extinction coefficient at the final range, $\sigma(r_f)$, must be known. Ferguson and Stephens (1983) used a novel iterative scheme in an attempt to select the value of $\sigma(r_f)$. The value of $\sigma(r_f)$ at a close-in range (where the returned signal is well above the system noise) was varied until the calculated extinction coefficients as a function of range $\sigma(r)$ allowed the calculated and measured lidar returns with range to agree. The chosen value of $\sigma(r_f)$ was then used as $\sigma(r_o)$ to integrate out from the transmitter. This technique, however, is limited to situations where the ratio of backscatter to extinction is a known constant along the path.

Solutions to the single-scatter lidar equation have been presented for reverse (Klett, 1985) and forward (Bissonnette, 1986) integration where the relationship between the backscatter and extinction coefficients is assumed to vary with range according to

$$\beta(r) = C(r)\sigma(r)^k \tag{11}$$

where k is a constant. For forward integration, the extinction coefficient as a function of range is given by

$$\sigma(r) = \frac{[1 - C(r)] \exp[S(r)]}{\dfrac{\exp[S(r_o)]}{C(r_o)\sigma(r_o)} - 2\displaystyle\int_{r_o}^{r} [1 - C(r)] \exp[S(r')]dr'} \tag{12}$$

and for reverse integration by

$$\sigma(r) = \frac{[1 - C(r)] \exp[S(r)]}{\dfrac{\exp[S(r_f)]}{C(r_f)\sigma(r_f)} + 2\displaystyle\int_{r}^{r_f} [1 - C(r)] \exp[S(r')]dr'} \tag{13}$$

where the constant k has been chosen to be unity. While these solutions allow for variable backscatter and extinction coefficients, their usefulness requires an *a priori* knowledge of the ratio $C(r)$ as a function of range. Salemink et al. (1984) determined values of σ and β from horizontal lidar shots by using the slope method when the atmosphere appeared to be horizontally homogeneous. They then presented a parameterization between values of β, σ and relative humidity ($33\% \leqq RH \leqq 87\%$). When the parameterization was used to invert visible wavelength lidar returns in the vertical direction, the derived extinction coefficient profiles (using radiosonde measurements of relative humidity) sometimes agreed reasonably well with those measured by aircraft mounted extinction meters. In contrast, de Leeuw et al. (1986) using similar types of lidar measurements did not observe a distinct statistical relationship between backscatter and extinction ratios and relative humidity. Fitzgerald (1984) pointed out that other factors, such as the aerosol properties, can strongly affect the relationship between β σ and relative humidity and that the power law relationship of Eq. 11 is not necessarily valid for relative humidities less than about 80%. A unique relationship between $C(r)$ and relative humidity which is dependent on the air mass characteristics is yet to be developed.

A lidar inversion algorithm using a double-ended lidar technique recently developed independently by two researchers (Paulson, 1986; Kunz, 1987). In this technique, the assumption concerning the relationship between the backscatter and extinction coefficients is eliminated by comparing the powers returned from a volume common to each of the two lidars located at opposite ends of the propagation path. However, the receiver gain of both lidars must be accurately known.

The mathematical formulation of the double-ended technique is as follows: Consider two lidars separated by a distance d. If we assign the origin of the propagation path to be located at lidar 1, the range-compensated power, $S(r)$, received by lidar 1 from a volume at range r is determined by the single-scatter lidar equation to be

$$S(r)_1 = \ln K_1 + \ln [\beta(r)] \quad 2 \int_o^r \sigma(r')dr' \tag{14}$$

and that received by lidar 2 is

$$S(r)_2 = \ln K_2 + \ln [\beta(r)] \quad 2 \int_r^d \sigma(r')dr' \tag{15}$$

Where K_1 and K_2 are the instrumentation constants for each of the lidars, and $\sigma(r)$ and $\beta(r)$ are the volumetric extinction and backscatter coefficients, respectively. If the scattering particles are assumed to be spherical, the backscatter coefficients are eliminated by subtracting Eq. 15 from Eq. 14, and we are left with

$$S(r)_1 \quad S(r)_2 = \ln (K_1 \quad K_2) \quad 2 \int_o^r \sigma(r')dr' + 2 \int_r^d \sigma(r')dr' \tag{16}$$

Since

$$\int_r^d \sigma(r')dr = \int_o^d \sigma(r')dr' - \int_o^r \sigma(r')dr' \tag{17}$$

Equation 16 becomes

$$S(r)_1 \quad S(r)_2 = \ln(K_1 \quad K_2) \quad 4\int_o^r \sigma(r')dr' + 2\int_r^d \sigma(r')dr' \tag{18}$$

Taking the derivative of Eq. 18 with respect to range, we obtain

$$\sigma(r) = \quad \frac{1}{4}\frac{d}{dr}[S(r_1) \quad S(r_2)] \tag{19}$$

The determined values of $\sigma(r)$ can then be used with the system constants in either Eq. 14 or Eq. 15 to determine the associated backscatter coefficients.

The double-ended technique has been used recently by Hughes and Paulson (1988) to examine the effects of spatial inhomogeneities on the single-ended lidar inversion algorithms. Measurements were made with two visioceilometer (Lindberg et al., 1984) lidars over a 0.9825-km slant path near the ocean on the Point Loma Peninsula in San Diego, California. Lidar 1 and lidar 2 were located approximately 38 meters and 135 meters above mean sea level, respectively. Each lidar was pointed about 3 or 4 meters away from the other's receiver, and the firings were offset in time by about 1 second to avoid amplifier saturations and signal contaminations. The data presented here are samples of two returns taken on 27 October 1986 during a period of reduced visibility and when conditions along the propagation path were observed to be varying both spatially and with time.

In Fig. 12a, the $S(r)$ values calculated from the individual lidar returns are shown. In each case the ranges are referenced to the location of lidar 1. Similarities in the larger atmospheric irregularities are evident in each data set. However, there are differences in the fine structure of the individual $S(r)$ curves which may be related to the slightly offset sampling volumes and firing times of the two lidars, as well as to the different background scenes viewed by each lidar. However, the background only adds a constant value to the observed backscatter signals. This contribution was found to be small in all cases, since the signal-to-noise ratio for both lidars exceeded 10 dB at a range of 800 meters. In any event, data-smoothing was necessary, and an 11-point (82.5-meter) running average of each $S(r)$ curve was determined before taking the differences. The differences in the smoothed $S(r)$ curves for each data set are then shown in Fig. 12b. The derivatives of the $S(r)$ difference curves were calculated with a running range interval of 15-points (112.5 meters), and the values of $\sigma(r)$, calculated from Eq. 19, are shown in Fig. 13a.

The corresponding backscatter coefficients, $\beta(r)$, are shown in Fig. 13 b. They were determined by using the calculated values of $\sigma(r)$ with the appropriate $S(r)$ values and system constants in either Eq. 14 or 15. The backscatter coefficients determined for lidar 1 and lidar 2 are in good agreement. The slight differences occurring within a range of 450 meters may reflect the precision with which both systems could be calibrated. Interestingly, the backscatter coefficients do not show the striking fluctuations of the extinction coefficients, which leads to the conclusion that $C(r)$ was not constant along the path. The ratios of the calculated extinction coefficient profiles and the backscatter coefficient profiles for lidar 2, $C(r)$, were determined (assuming the value of k in Eq. 11 to be unity) and are presented in Fig. 13c.

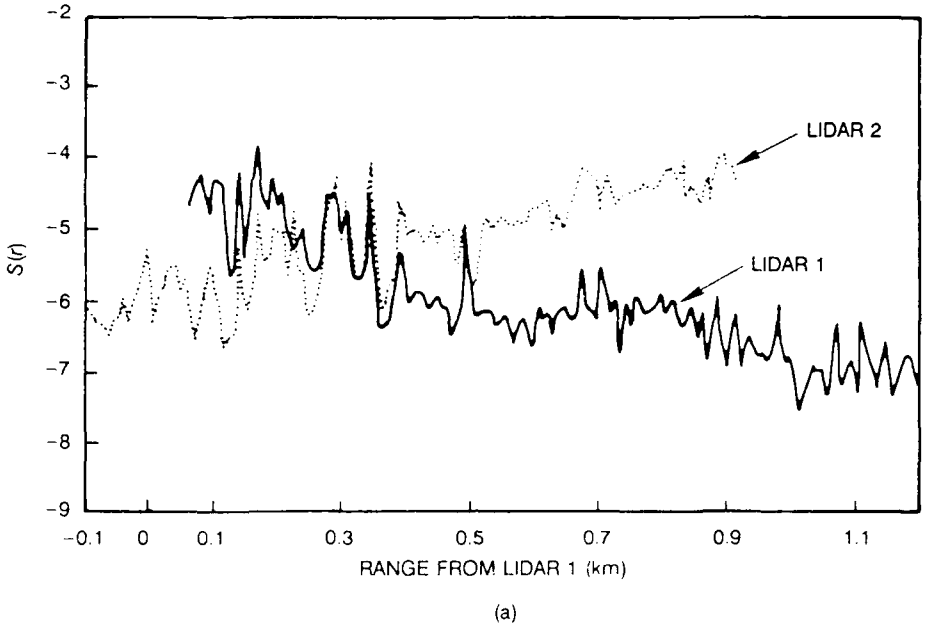

(a)

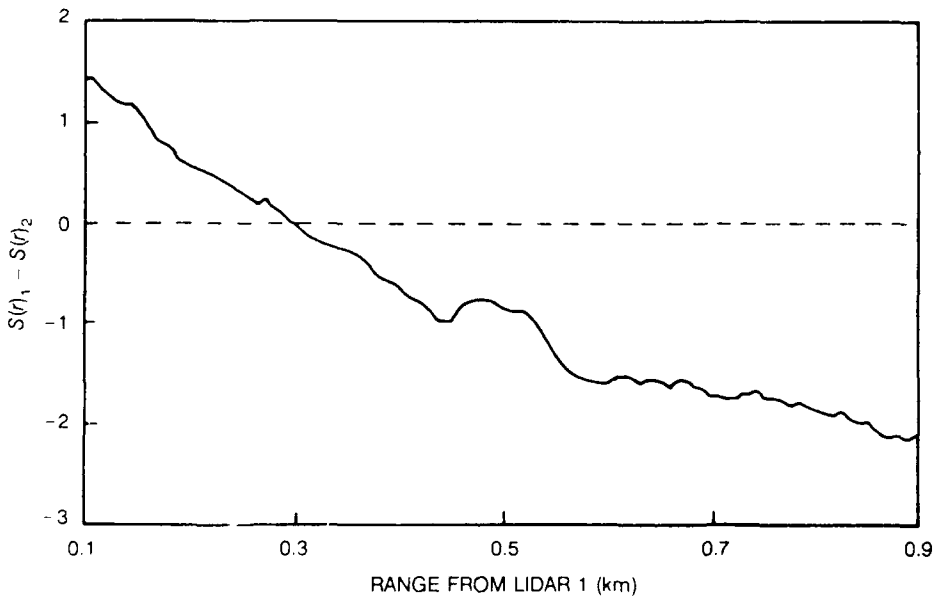

(b)

Figure 12. Comparison of range-compensated power return, $S(r)$, for (a) lidar 1 and 2 and (b) their differences in range from lidar 1.

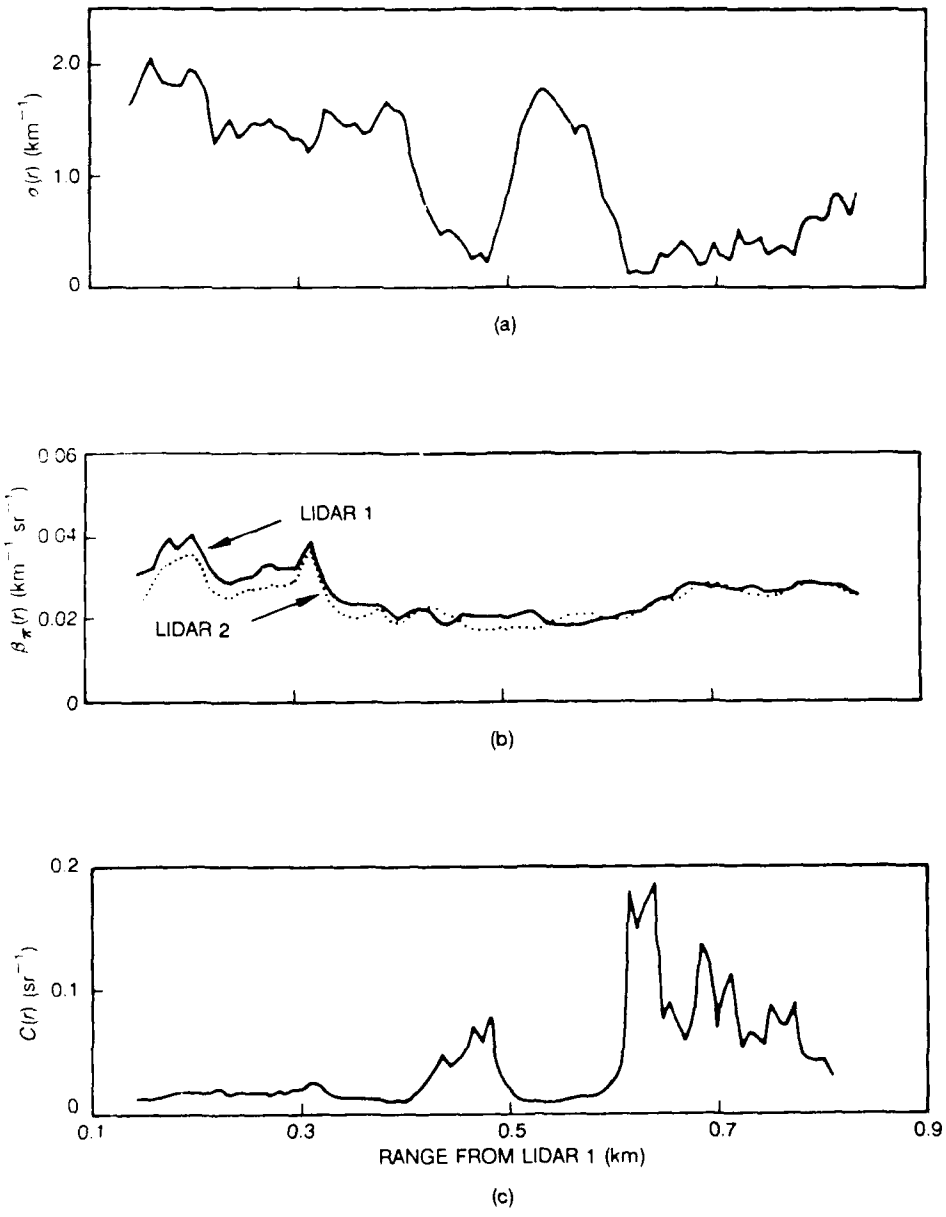

Figure 13. Comparison of calculated (a) extinction coefficient $\sigma(r)$, (b) backscatter coefficient $\beta(r)$, and (c) backscatter/extinction ratio $C(r)$ vs. range from lidar 1.

Extinction coefficients were calculated as a function of range for forward and reverse integration by using the individual lidar returns, and were then compared with those determined by the double-ended technique when $C(r)$ was assumed to be either a constant or allowed to vary with range according to Fig. 13c. The results of the double-ended lidar technique provide the close-in or far-away boundary values for each lidar.

Figure 14a shows the comparisons for forward integration determined when $C(r)$ is assumed to be constant over the propagation path. There is little or no agreement between the extinctions determined by either lidar and those of the double-ended measurements, even though the boundary values were specified. Near a range of 600 meters, where the values of $C(r)$ increase (Fig. 13c), the extinctions by lidar 1 exhibit the well-known "instabilities" in that they tend to increase without bound. The extinctions by lidar 2 also exhibit the instabilities by tending to zero at the farther ranges. These data demonstrate the sensitivity of the instabilities to the magnitudes of the boundary values.

Figure 14b shows the comparisons for reverse integration when $C(r)$ is assumed to be constant. Although the solutions are "stable," there is little agreement between the double-ended measurements and the extinctions determined by either lidar.

If the values of $C(r)$ are allowed to vary with range, as shown in Fig. 13c, excellent agreements are obtained between the calculated extinction coefficients of lidars 1 and 2. The extinction coefficient profiles for both the forward (Fig. 15a) and reverse (Fig. 15b) integrations are nearly identical with the corresponding double-ended measurements shown in Fig. 13a.

These results demonstrate that if the value of $C(r)$ varies with range, but is assumed to be a constant, neither the single-ended forward or reverse integration algorithms will allow range-dependent extinction coefficients to be determined with any assured degree of accuracy even if the initial boundary values are specified. If, however, the manner in which $C(r)$ varies is specified, both the forward and reverse single-ended inversions for this data set reproduce the double-ended measurements remarkably well. Whether the same is true for other situations needs to be determined.

If the conditions under which the forward inversion algorithm is stable can be established, then a single-ended lidar inversion technique would be possible when augmented with a close-in measurement of extinction and measurements to relate $C(r)$ to air mass characteristics and relative humidity.

While the works of Mulders (1984) and de Leeuw et al. (1986) have concluded that no relationship exists between $C(r)$ and relative humidity, their measurements did not account for changes in the air mass characteristics. Whether or not such a relationship can ever be identified in a practical sense is yet to be determined.

In situations where the different layers of the atmosphere are horizontally homogeneous, the need for knowing the relationship between the backscatter and extinction coefficients can be eliminated by comparing the range-compensated powers received from each altitude along two or more different elevation angles (Russel and Livingston, 1984; Paulson, 1989). Assuming the atmosphere to be horizontally homogeneous with extinction and backscatter coefficients, $\sigma(h)$ and $\beta(h)$, respectively, which vary only in the vertical direction, the powers received from an altitude h_1 along a slant path r_1 elevated ϕ_1 degrees and along a slant path r_2 elevated ϕ_1 degrees (Fig. 16) are given by

$$P(r_1) = \frac{K\beta(h_1)}{(h_1 \csc \phi_1)^2} \exp\left[2\int_0^{h_1} \sigma(h')dh' \csc \phi_1\right] \tag{20}$$

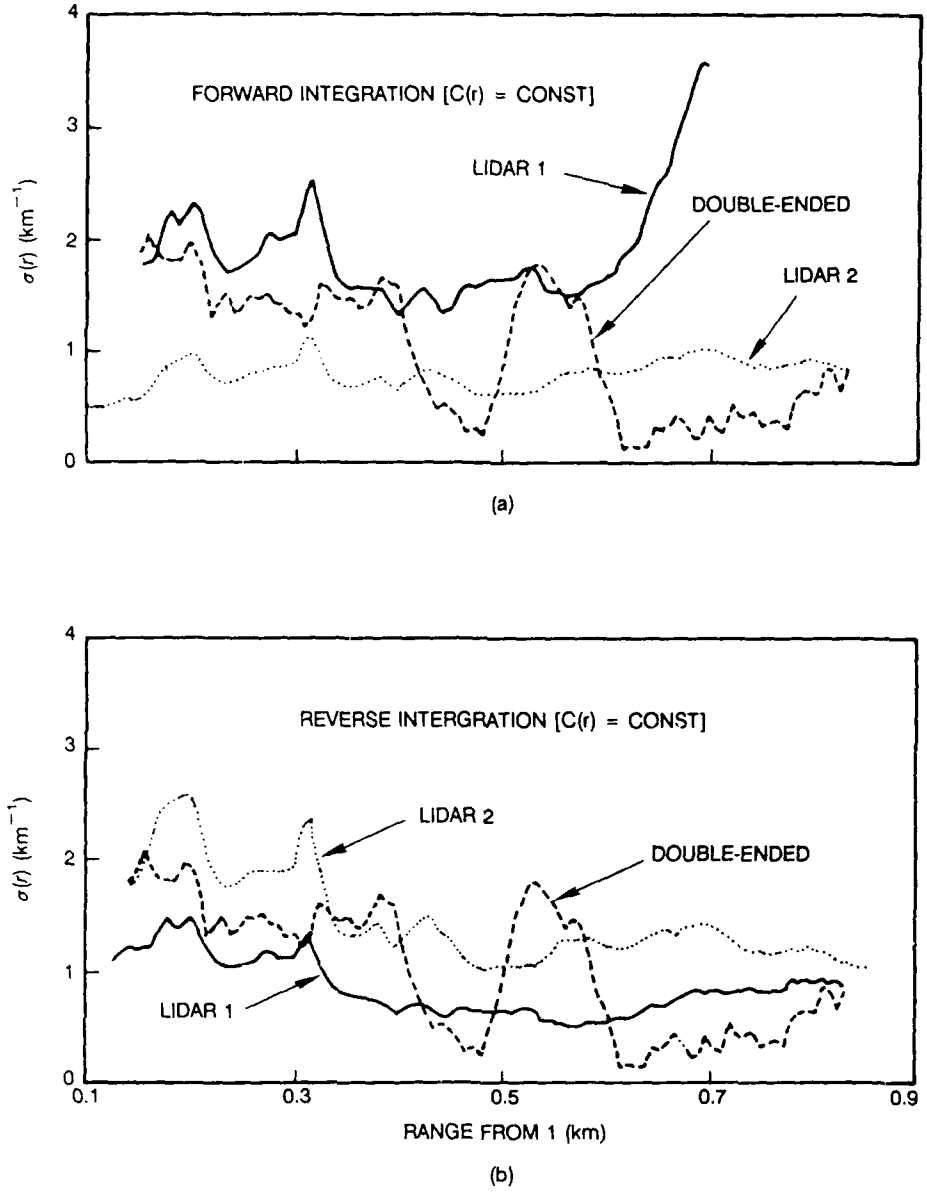

Figure 14. Comparison of extinction coefficients $\sigma(r)$, vs. range from lidar 1 calculated from lidars 1 and 2 by using (a) forward and (b) reverse integration and those using the double-ended technique when $C(r)$ is assumed to be constant.

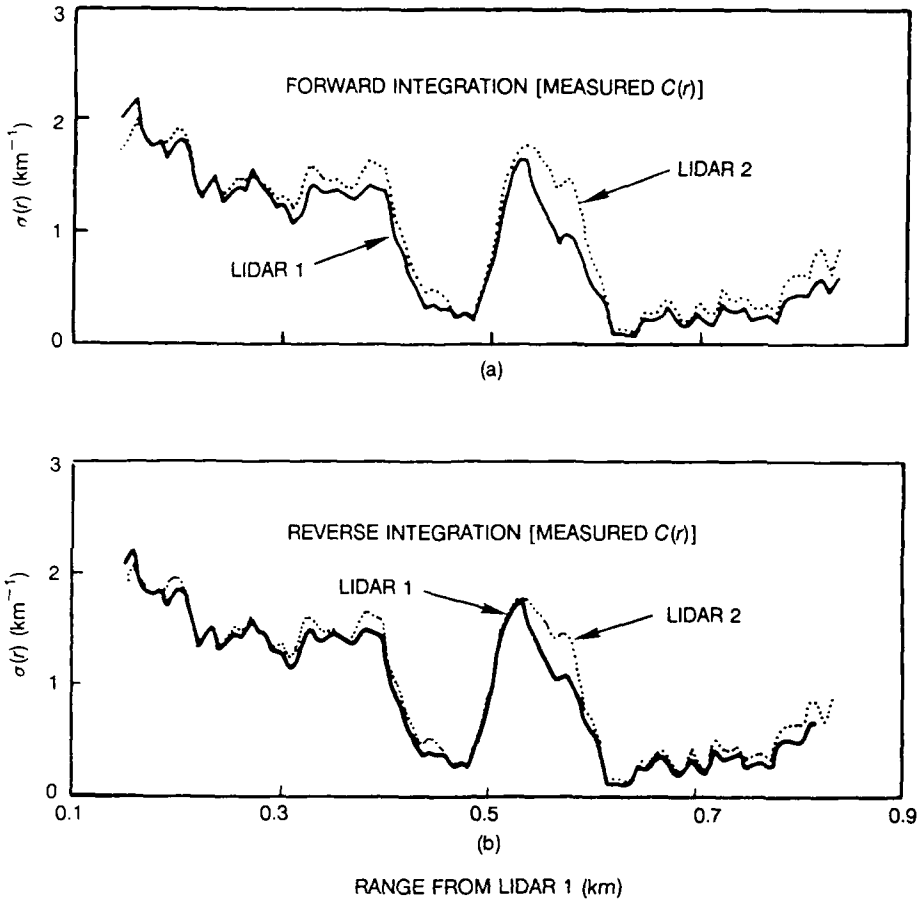

Figure 15. Comparison of extinction coefficients σ (r) vs. range from lidar 1 calculated from lidars 1 and 2 by using (a) forward and (b) reverse integration when $C(r)$ is allowed to vary as measured.

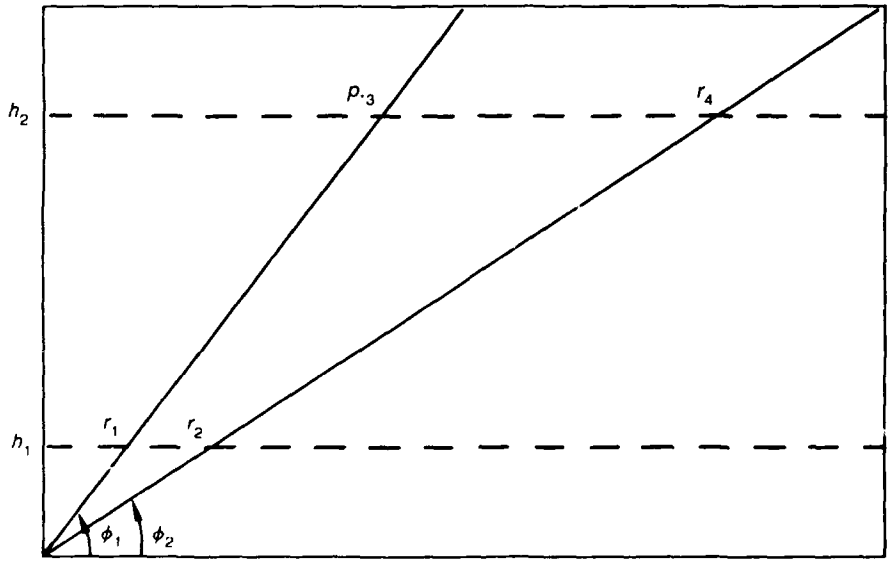

Figure 16. Geometry for the two-elevation-angle lidar technique.

and

$$P(r_2) = \frac{K\beta(h_1)}{(h_1 \sin \phi_2)^2} \exp\left[-2\int_0^{h_1} \sigma(h')dh' / \sin \phi_2\right] \tag{21}$$

where K is the system constant. Dividing Eq. 20 by Eq. 21, we get

$$\frac{P(r_1)(h_1 \sin \phi_1)^2}{P(r_2)(h_1 \sin \phi_2)^2} = \exp\left[-2\left(\frac{1}{\sin \phi_1} - \frac{1}{\sin \phi_2}\right)\int_0^{h_1} \sigma(h')dh'\right] \tag{22}$$

or, taking the logarithm of both sides

$$\ln\left[\frac{P(r_1)(h_1 \sin \phi_1)^2}{P(r_2)(h_1 \sin \phi_2)^2}\right] = -2\left(\frac{1}{\sin \phi_1} - \frac{1}{\sin \phi_2}\right)\int_0^{h_1} \sigma(h')dh' \tag{23}$$

and

$$\int_0^{h_1} \sigma(h')dh' = \frac{S(r_1) - S(r_2)}{2(1/\sin \phi_2 - 1/\sin \phi_1)} \tag{24}$$

where

$$S(r) = \ln[P(r)(h \sin \phi)^2] \tag{25}$$

Similarly

$$\int_0^{h_2} \sigma(h')dh' = \frac{S(r_3) - S(r_4)}{2(1/\sin \sigma_2 - 1/\sin \phi_1)} \tag{26}$$

Then

$$\tau_a = \int_{h_1}^{h_2} \sigma(h')dh' = \int_0^{h_2} \sigma(h')dh' - \int_0^{h_1} \sigma(h')dh'$$

$$\tau_a = \frac{[S(r_3) - S(r_4)] - [S(r_1) - S(r_2)]}{2(1/\sin \phi - 1/\sin \phi_1)} \tag{27}$$

In principle, if the atmosphere were horizontally homogeneous, the lidar beam could be swept in elevation and an incremented profile of extinction (and consequently backscatter) could be determined by using the returns from closely separated angles (Kunz, 1988). The smaller angular separations, however, place stringent requirements on the accuracies to which the range-compensated powers must be measured. If we assume that the percentage errors, δ, in the $S(r)$ values are equal, the percent error, $\Delta\tau_a$, in the calculated optical depths is

$$\Delta\tau_a = [(\tau_a' - \tau_a)/\tau_a] \times 100 \tag{28}$$

where τ'_0 is given by

$$\tau'_0 = \frac{\{[S(r_3)(1\pm\delta)] \quad [S(r_4)(1\pm\delta)]\} \quad \{[S(r_1)(1\pm\delta)] \quad [S(r_2)(1\pm\delta)]\}}{2(1 \sin \phi_2 \quad 1 \sin \phi_1)} \tag{29}$$

Where $(\tau'_0 \quad \tau_0)$ is a maximum, the signs of δ are such that the products of $S(r)(\pm\delta)$ are all of the same sign; then

$$\tau'_0 \quad \tau_0 = \frac{\pm[S(r_3) + S(r_4) + S(r_1) + S(r_2)]\delta}{2(1 \sin \phi_2 \quad 1 \sin \phi_1)} \tag{30}$$

To demonstrate this worst-case condition, the extinction coefficient is allowed to vary linearly from a value of 0.05 km $^{-1}$ at the surface to 1.0 km $^{-1}$ at a height of 1 km. Assuming that the relationship between backscatter and extinction were invariant with altitude (i.e., $C(r) = C$), $S(r)$ values were calculated for heights of 0.1 km and 1 km for elevation angles of $\phi_1 = 60$ degrees and $\phi_2 = 30$ degrees. The sensitivity of the optical depth to uncertainties in the $S(r)$ values is shown in Fig. 17 for $\ln(KC) = 0$ and -5.4, which demonstrates that the errors are are also dependent upon the relationship between backscatter and extinction. In both cases, the sensitivity of the optical depth to errors in $S(r)$ measurements is readily apparent.

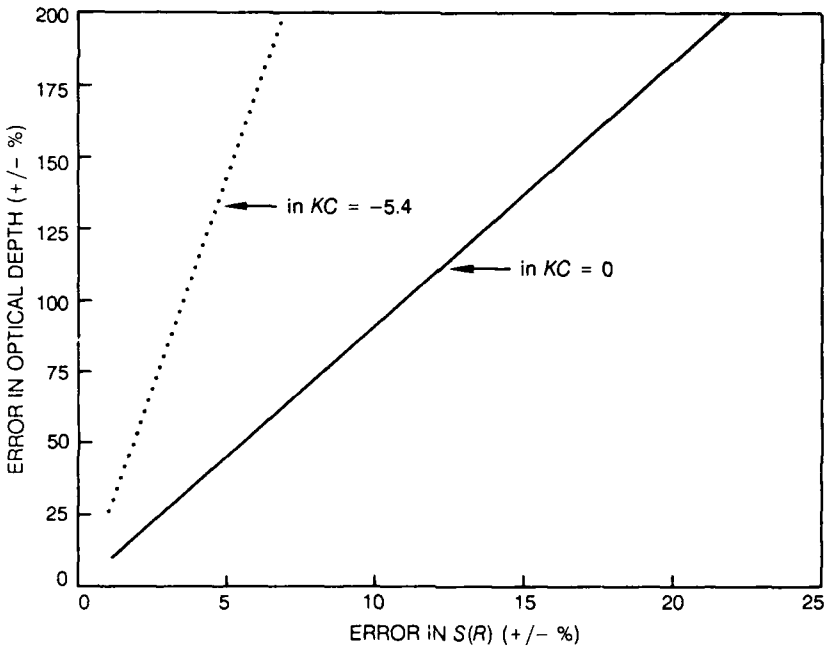

Figure 17. Errors in optical depths as a function of errors in $S(r)$ measurements for an extinction coefficient profile which varies linearly from 0.05 km^{-1} at the surface to 1 km^{-1} at a height of 1 km for different products of system constant K and backscatter-to-extinction ratio C.

The extent to which the atmosphere is horizontally homogeneous could be determined from a single horizontal lidar shot by examining the gradient of the range-compensated power return. Then, if the atmosphere appeared homogeneous, i.e., a constant negative gradient in $S(r)$, the optical depth between any two altitudes could be determined from Eq. 27. However, the atmosphere within the convectively mixed marine boundary layer rarely, if ever, has the degree of homogeneity required. Paulson (1989) has recently conducted an investigation as to the usefulness of the two-angle lidar technique in a coastal region. In these studies, data were taken beneath a thin stratus cloud layer at about 500 meters. Two visioceilometer lidars were operated side-by-side on the west side of the Point Loma Peninsula and pointed west overlooking the Pacific Ocean. A series of nearly simultaneous shots were made with this arrangement. Without changing the orientation, the elevation angle of lidar 1 was increased to 25 degrees and that of lidar 2 to 50 degrees. A series of nearly simultaneous shots were also made with this configuration.

Examples of the horizontal range-compensated power returns, $S(r)$, for a 5-point running average for each lidar are shown in Fig. 18. The two lidar returns are in quite good agreement, but the irregularities and increasing return with increasing range indicate an inhomogeneous condition. The $S(r)$ data plotted as a function of altitude for the two-angle shots are shown in Fig. 19. The effects of the inhomogeneities are evidenced by the fluctuations in the $S(r)$ curve for lidar 1 above and below that for lidar 2 at different ranges. The optical depths between different altitudes determined from Eq. 27 are shown in the following table:

Table 1. Optical depths calculated from different altitudes up to a maximum altitude of 475 meters on 17 May 1989.

Lower Altitude (m)	Optical depth
100	0.811
125	0.437
150	0.584
175	0.597
200	0.647
225	0.584
250	0.688
275	0.150
300	0.260
325	0.260
350	0.342
375	0.492

The optical depth between 275 and 475 meters is only 0.15, while that from 375 to 475 meters is more that three times greater (0.49). If the data were representative of a horizontally homogeneous condition, the optical depth up to 475 meters should consistently decrease as h_1 increases.

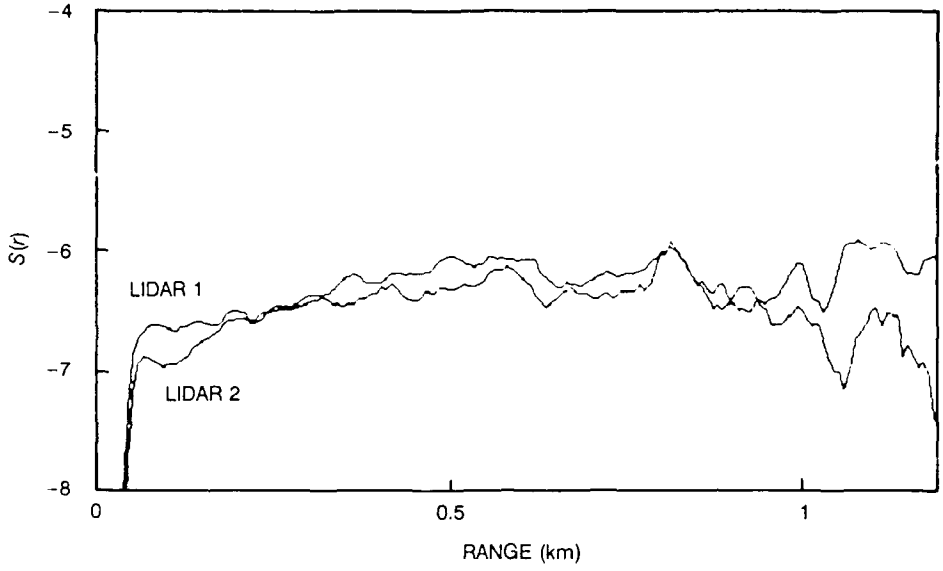

Figure 18. Examples of measured $S(r)$ values obtained from parallel horizontal lidar shots for lidars 1 and 2 with a 5-point running average.

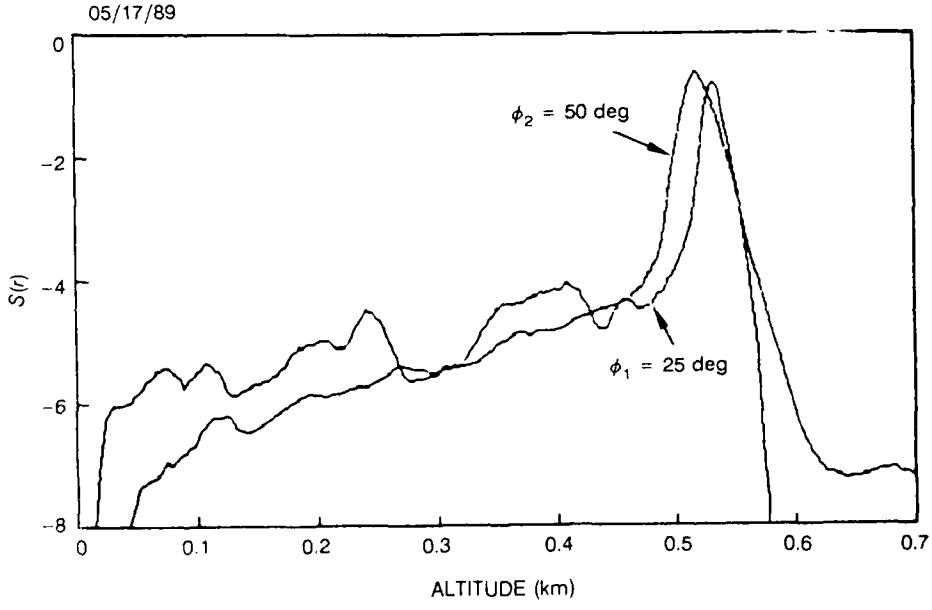

Figure 19. Examples of two-elevation-angle lidar shots (ϕ_2 = 25 degrees and ϕ_2 = 50 degrees) with a 5-point running average.

ASSESSMENT OF SYSTEM PERFORMANCE

The computer code PREOS (Performance and Range for EO Systems) presently resides in the US Navy's Tactical Environmental Support System (TESS). The present version of PREOS addresses the ability of FLIR systems on the S3-A, A-6, and P-3 operational aircraft to perform range-dependent tasks such as the detection, classification, and identification of surface targets. The code utilizes polynomial fits calculated with LOWTRAN 3B (Selby et al., 1976) of equivalent gaseous absorber amounts based on meteorological parameters. The aerosol transmittance model in PREOS was developed from a model obtained from the work of B.A. Katz at the Naval Surface Warfare Center (see Hughes and Richter, 1979). This model employs height-dependent marine and continental components. In a manner similar to the LOWTRAN 6 NAM, the marine contribution is scaled to surface wind speed, and both contributions contain relative humidity particle-size growth factors.

The agreement between surface target detection ranges as reported by operational squadrons and those predicted by the code has been disappointing. However, the wide scatter between observed and predicted ranges (Fig. 20) is probably more characteristic of operator capability and the quality of input data than the predictive capability of the model. The meteorological inputs to the code were obtained in many instances from radiosonde launches which may have occurred several hundred kilometers from the observation sites and may have been separated in time by several hours. Predictions of performance range are also critically dependent upon the actual temperature of the ship and of its natural background. The algorithms in PREOS are currently based on a fixed temperature difference between a rectangular target and its natural background. This approach neglects the effects of a wind-ruffled sea on sky reflections, emissions from the surface wave facets, and contributions of the intervening atmosphere to the total background radiance scene, which changes with viewing angle and the altitude of the sensor. Without knowing the ship's temperature, which is dependent upon its history (course, speed, and surrounding meteorological parameters), it is questionable that the accuracy of detection range against an adversary can be much improved. However, a ship commander, when aware of his own ship's past and future courses, can use the prediction algorithms to determine the ranges at which an adversary can detect or track the ship using passive IR sensors. These stand-off ranges are of primary importance in estimating the time allowable for evasive actions against guided weaponry launched at the ship or for the deployment of countermeasures.

Currently available computer codes, such as SIREOS (Burns et al., 1980) (three-dimensional) and SIRS (Batley, 1978) (two-dimensional), are capable of using several hundred individual structural elements of a ship to model its composite IR signature. These codes, however, are quite complex and require extensive running times, making them impractical for shipboard use in a real-time prediction system. A modification to the SIRS computer code has recently been developed at the Naval Surface Weapons Center. This modification, SHIPSIG (Ostrowski and Wilson, 1985), approximates the complex structure of a ship with plane elements which represent the ship's temperature at zero-range on an average basis. For a given viewing direction, the simplest representation of the ship consists of a single vertical and horizontal element, with the observer's orientation accounted for by appropriate area components. In the present model, the horizontal and vertical elements and ship-stack correction factors apply to a guided missile frigate-class ship. The model requires as inputs the ship's course and speed as a function of time from a starting geographic latitude, the surface wind speed and direction, visibility, relative humidity, air temperature, the ship's initial temperature, and the viewing angle.

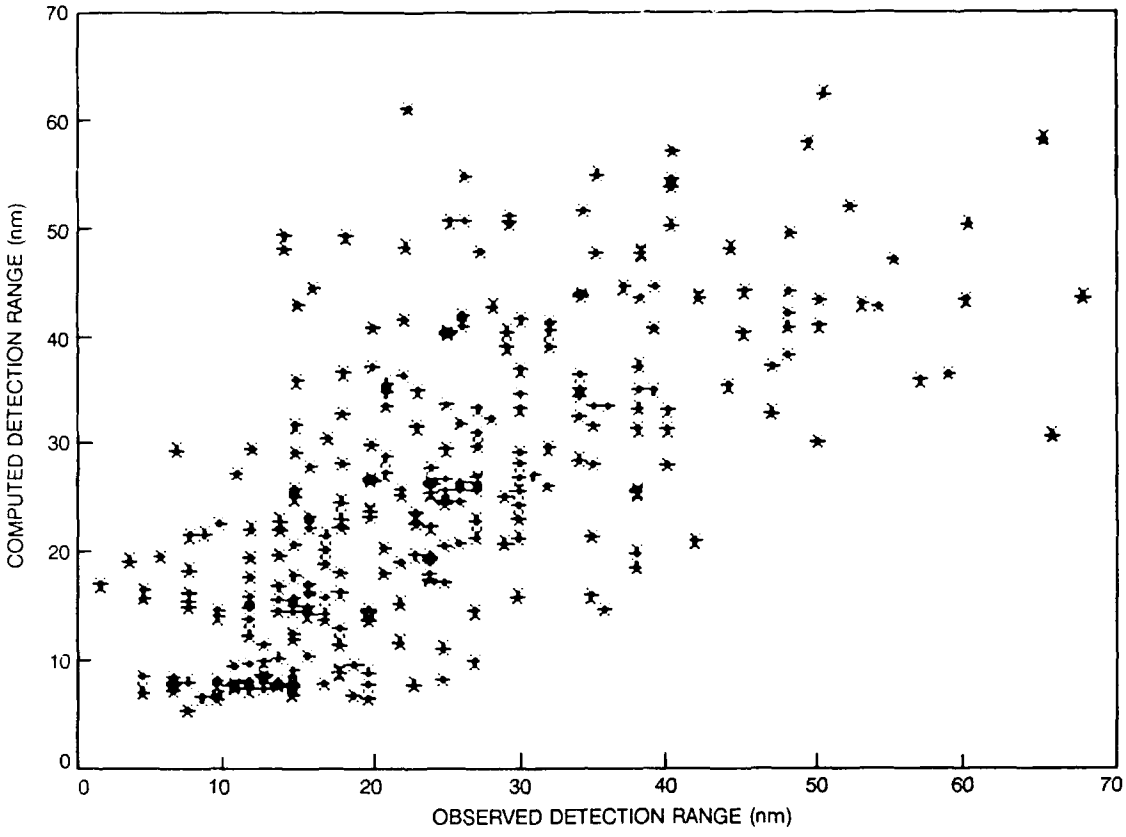

Figure 20. Comparison of observed FLIR detection ranges and those predicted by PREOS.

A FLIR detection algorithm has recently been developed (Hughes, 1989c) by using the SHIPSIG model and the sea surface background model, which varies with sensor altitude and viewing (zenith) angle. As neither model has undergone extensive validation, the algorithm is not yet incorporated into the operational version of PREOS. To demonstrate the use of the algorithm as a tactical decision aid to predict the vulnerability of a frigate-class ship to detection by an airborne common module FLIR, a case study is presented (using the actual course of a frigate operating off the coast of San Diego, California). During a 5-hour period the ship's course changed, allowing solar heating of different sides of the ship.

For this study, the Piper Navajo aircraft made a vertical spiral in the vicinity of the ship to obtain the profile of temperature, relative humidity, and pressure, which are required inputs to the modified LOWTRAN 6 computer code for calculating the sea and sky radiances. A Barnes PRT-5 radiation thermometer was also onboard the aircraft to measure sea surface temperature from low-level constant-altitude flights; the temperature was determined to be 16.4°C. The vertical profiles of temperature and relative humidity, which were measured at 1330 PST approximately 9 km off the coast of San Diego, California, are shown in Fig. 21.

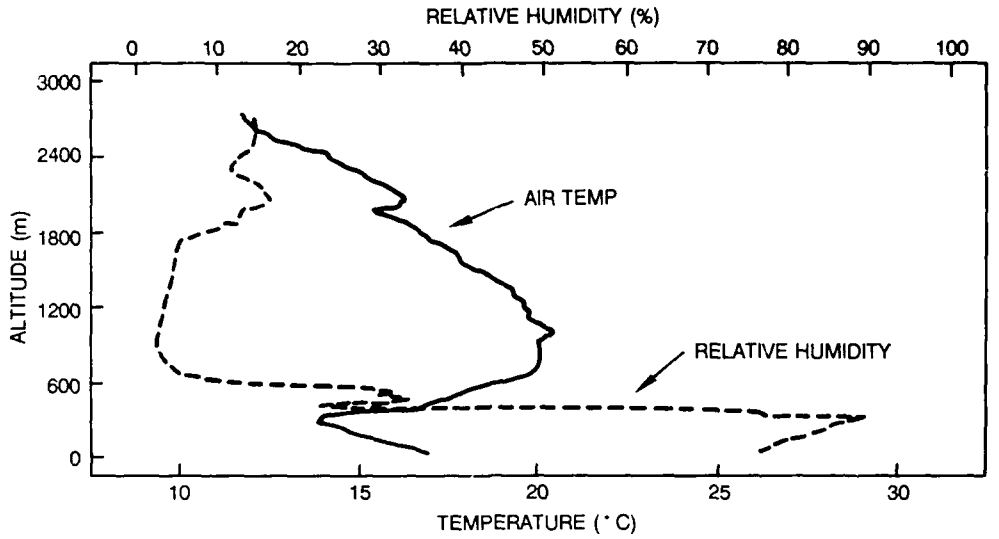

Figure 21. Profiles of air temperature and relative humidity measured with altitude on 9 June 1988 off the coast of San Diego, California.

Near the time the meteorological parameters were obtained, measurements of 8–12-μm horizon radiances were made with the thermal imaging system (AGA THERMOVISION, model 780). The current and 24-hour averaged wind speeds (V_c = 2.9 m/s and $\bar{V}$ = 2.8 m/s) and the vertical profiles of meteorological parameters were used in LOWTRAN 6 to calculate the radiance that matched the maximum radiance in the scene for nonunique combinations of air mass factors and visibilities. At the time of the measurements, the Los Coronodos coastal islands off San Diego were barely visible to the naked eye at ranges between 25 and 35 km. Choosing a visibility of 37 km, an integer value of 3 resulted as the appropriate air mass factor for the LOWTRAN 6 NAM. Figure 22 shows the comparison of the measured and calculated IR radiances for zenith angles within about 1 degree above and 1 degree below the horizon, with an air mass factor of 3 and a visibility of 37 km. Both the calculated sky ($\theta < 90.17$ degrees) and sea ($\theta > 90.17$ degrees) radiances are in good agreement with the measured values for this low-wind-speed case.

The selected atmospheric model was used to calculate the contributions of the propagation path and sea and reflected sky radiances to the total background radiance as a function of altitude and zenith angle. In Fig. 23 the total apparent blackbody temperature of the sea background from the three contributors is plotted versus zenith angle for sensor altitudes of 500 meters and 2000 meters. At the 500-meter elevation, the dip in temperature at about 97 degrees is a result of the rapid fall-off of propagation path emission with increasing zenith angle (i.e., shorter slant paths to earth than at the 2000-meter elevation). For zenith angles greater than about 100 degrees, there is little difference in the apparent temperatures at each altitude, and both approach the measured sea surface temperature at the nadir zenith angle. This is in contrast to Fig. 10, where propagation path emissions between the sensor and sea surface made significant contributions to the total radiance at the nadir zenith angle for both at an altitude of 1000 meters.

Figure 24 shows the course of the guided missile frigate USS *Brooke* (FFG1) off the coast of San Diego, California, on 9 June 1988; this course was chosen to demonstrate

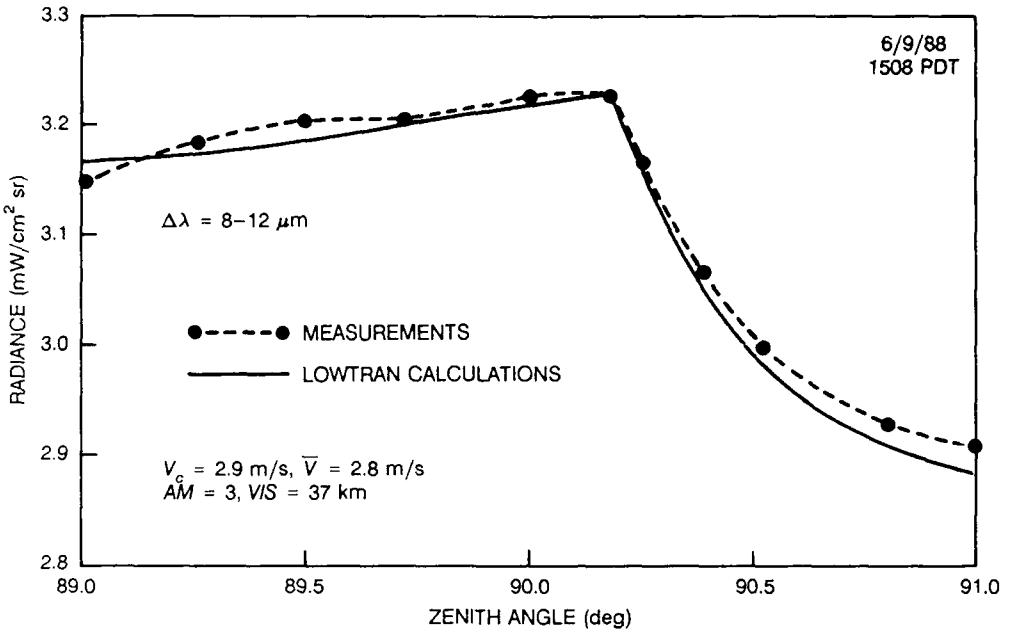

Figure 22. Comparison of measured and calculated IR radiances for zenith angles above (θ < 90.17 degrees) and below (θ > 90.17 degrees) the horizon.

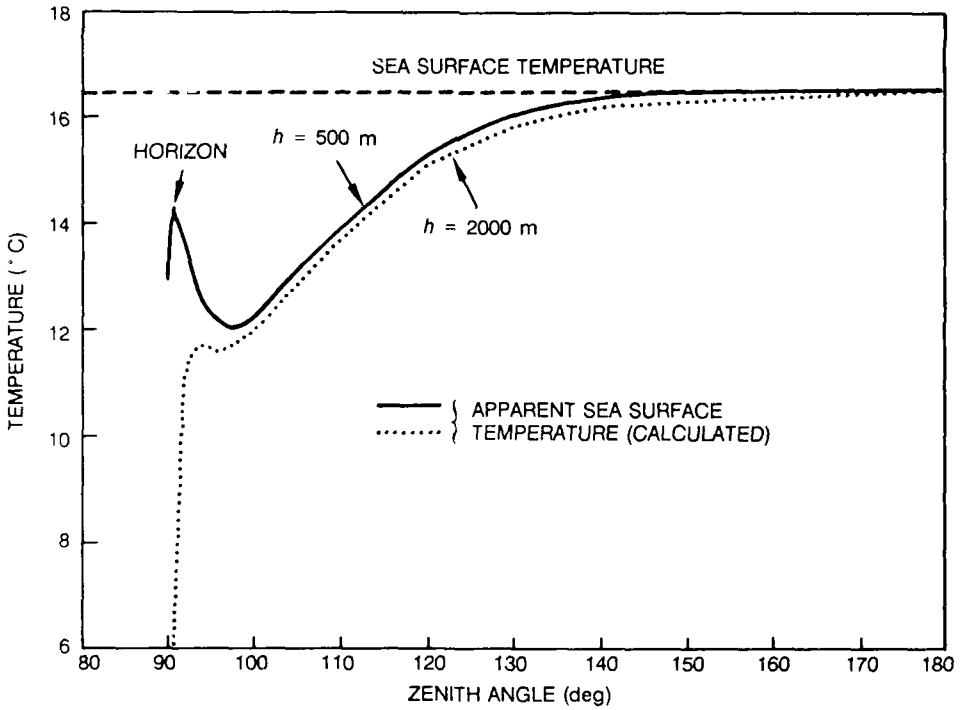

Figure 23. Total apparent blackbody temperature of the sea background versus zenith angle for sensor altitudes of 500 meters and 2000 meters.

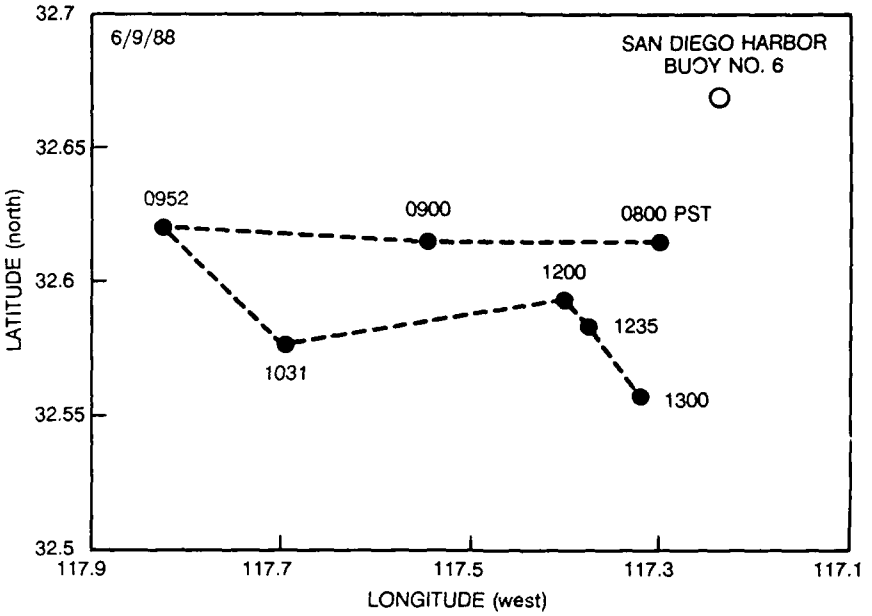

Figure 24. Course of the USS *Brooke* (FFG1) on 9 June 1988.

the model. During the 5-hour time period, changes in the ship's heading allowed solar heating of different sides of the ship. As the ship completed the course and returned to harbor, it passed close to the AGA thermal imaging system located near the entrance to the harbor. The AGA system's data processing software allows subtraction of the sea background radiance surrounding the ship and provides a histogram of the temperature distribution of the ship pixels within the chosen rectangular area. The mean temperature of the ship (uncorrected for atmospheric effects) was 19.7°C. The measured radiance, N(meas), of the ship at a range r is related to its actual effective blackbody radiance, N(ship), and the atmospheric emission, N(path), along the path by

$$N(\text{meas}) = N(\text{ship})\tau(r) + N(\text{path}) \tag{31}$$

where $\tau(r)$ is the atmospheric transmittance at a range r. The range to the ship, determined by using the known vertical dimensions of the ship and their angular subtense within the field-of-view of the AGA, was approximately 1.7 km. LOWTRAN 6 calculations of transmittance and path emission were made to determine the temperature equivalent to N(ship). These calculations resulted in an adjusted AGA average temperature measurement of 20.5°C, assuming that the surface emissivity of the ship was unity.

For the ship model calculations, the ship's initial position was taken to be near the entrance to San Diego harbor. The initial ship temperature, the ambient temperature, and the relative humidity throughout the course were not recorded by the ship. These values were taken to be constants as measured at the AGA site. The surface wind was southwesterly (252 degrees true), and the depression angle of viewing was essentially broadside at 0.6 degree. The average ship temperatures calculated for the port and starboard sides of the ship as a function of time are shown in Fig. 25. The most apparent features in the temperature responses are the rapid heating of the port side and the gradual cooling of the starboard side as the ship steamed westward in the early morning, and their abrupt cooling

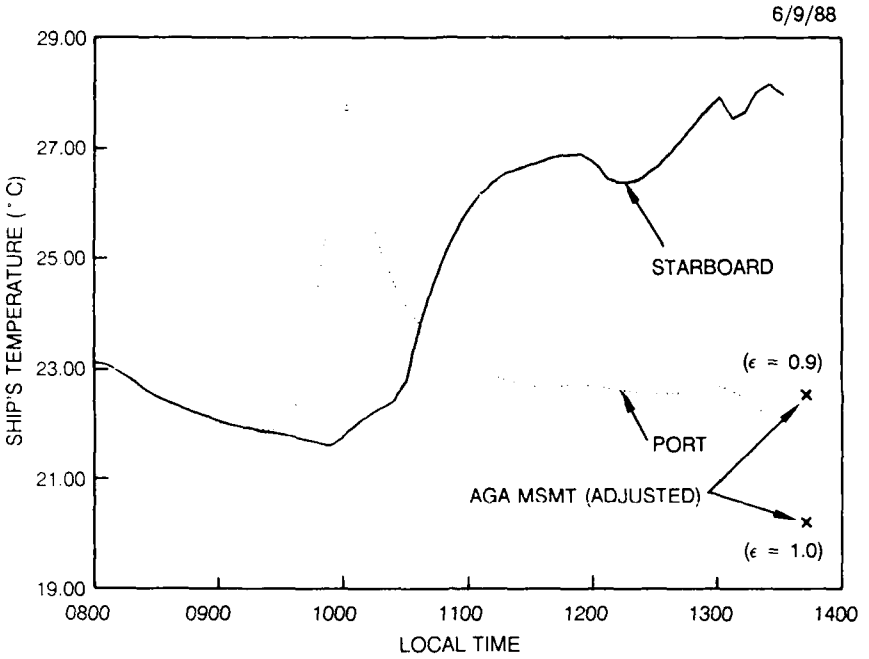

Figure 25. Average temperature of port and starboard sides of the USS *Brooke* (FFG1) and the adjusted AGA measurements as the ship entered San Diego harbor.

and heating after 1000 hours following the southeasterly course change at 0952 hours. The magnitude of the port side average temperature is approximately 1°C greater (for an emissivity of unity) than that measured by the AGA system as the ship returned to harbor near 1345 hours. If indeed the emissivity, ϵ, of the ship was 0.9, as is assumed in the model, the measured average temperature would be in better agreement (22.7°C). Allowing for the uncertainties in the meteorological parameters surrounding the ship throughout the course, the reasonable agreement between the adjusted AGA measurements and the model predictions is gratifying.

In the performance calculations, the LOWTRAN 6 code is used to directly calculate the sum of the ship and path radiances received by the sensor at a range r as

$$N(r)_{s+p} = N(r = 0)_s \tau(r) + N(r)_p \tag{32}$$

where $N(r = 0)_s$ is the ship radiance at zero range and $N(r)_p$ is the path radiance. $N(r)_{s+p}$ is then converted to an equivalent blackbody temperature, $T(r)_{s+p}$, by an iterative solution to Planck's blackbody formula. Similarly, an equivalent blackbody temperature, $T(r)_b$, of the background radiance at the specified altitude and range is calculated, and the resulting apparent temperature difference, $\Delta T(r)_a = T(r)_{s+p} \quad T_b(r)$, is determined. The range at which the apparent temperature difference is equal to the system's minimum detectable temperature difference (MDTD) curve determines the maximum detectable range (MDR) of the ship. The FLIR system MDTD versus range (spatial frequency) curve was calculated by using the formulation for a hypothetical ship operating against a rectangular target. In Fig. 26 and 27, the calculated MDRs for the USS *Brooke* by an airborne FLIR operating at altitudes of 0.5 km and 1.0 km, respectively, are shown. The MDRs could have been

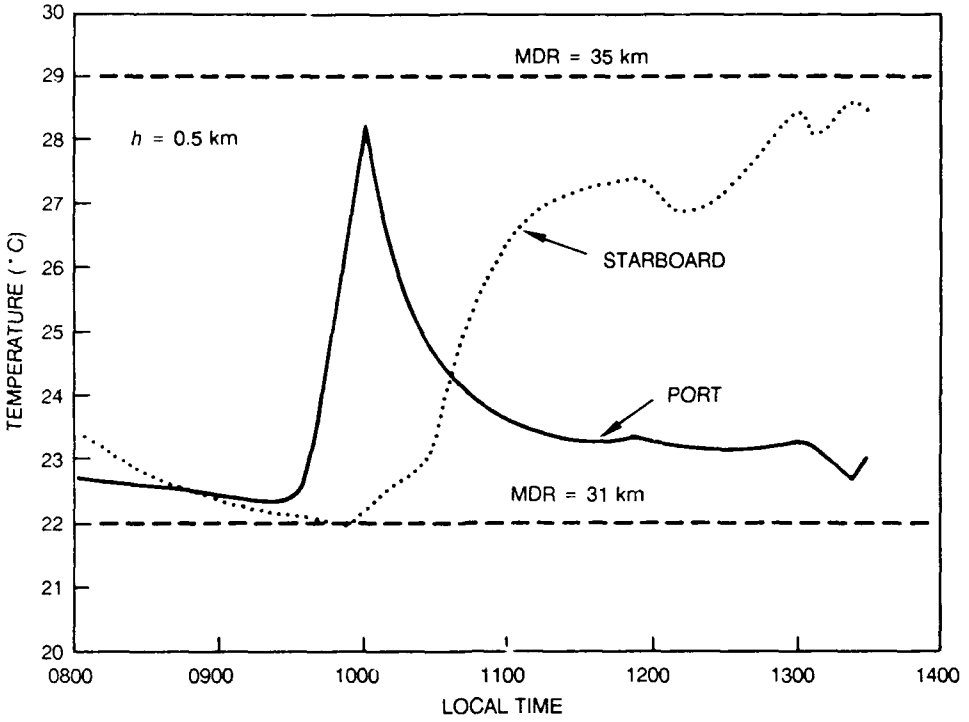

Figure 26. Calculated MDR envelopes for the USS *Brooke* (FFG1) by an airborne FLIR at an altitude of 0.5 km.

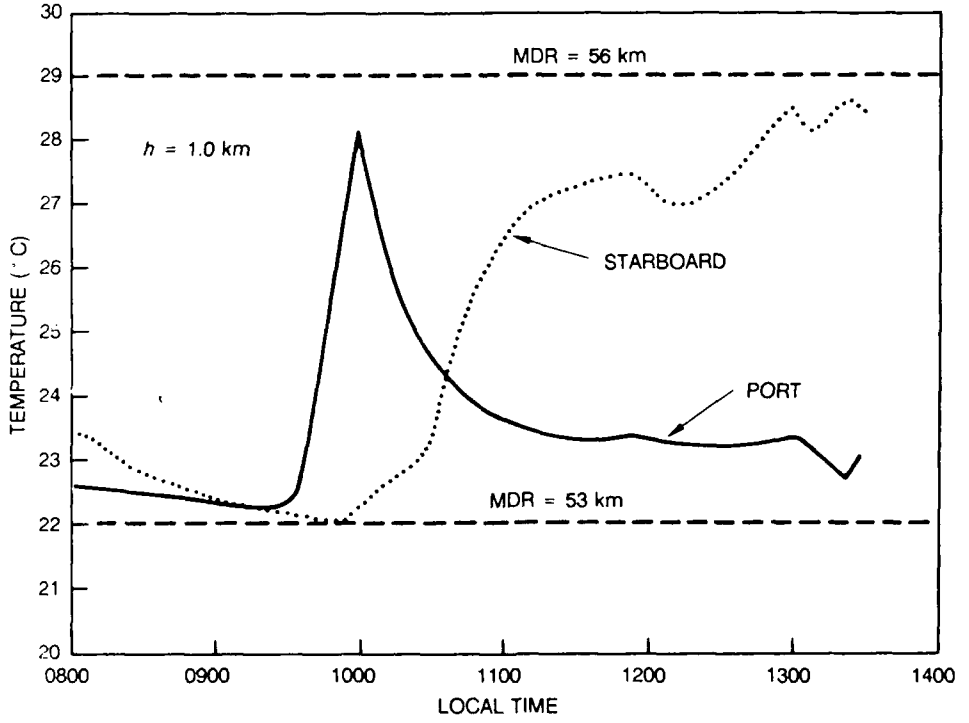

Figure 27. Calculated MDR envelopes for the USS *Brooke* (FFG1) by an airborne FLIR at an altitude of 1.0 km.

calculated as a function of time throughout the the ship's course; however, for the sake of simplicity, only the vulnerability detection envelopes for the entire duration of the ship's course are shown. In the figures, the ship's average temperature for both the port and starboard sides are shown. In Fig. 26, the ship is seen to be vulnerable to IR detection throughout its course from an altitude of 0.5 km at a range of 31 km. However, beyond 35 km the ship is not detectable. Similarly, in Fig. 27, the ship is vulnerable at a range of 53 km from an altitude of 1.0 km, but is safe from detection beyond 56 km. In Fig. 28 a comparison is shown of the MDRs calculated with the current algorithm and with the method that assumes a constant temperature difference between the ship and its background of 5 °C. When the current method is used, considerable increases (≈20 km at an altitude of 2.0 km) are obtained compared to the fixed-temperature method in predicted detection ranges with altitude.

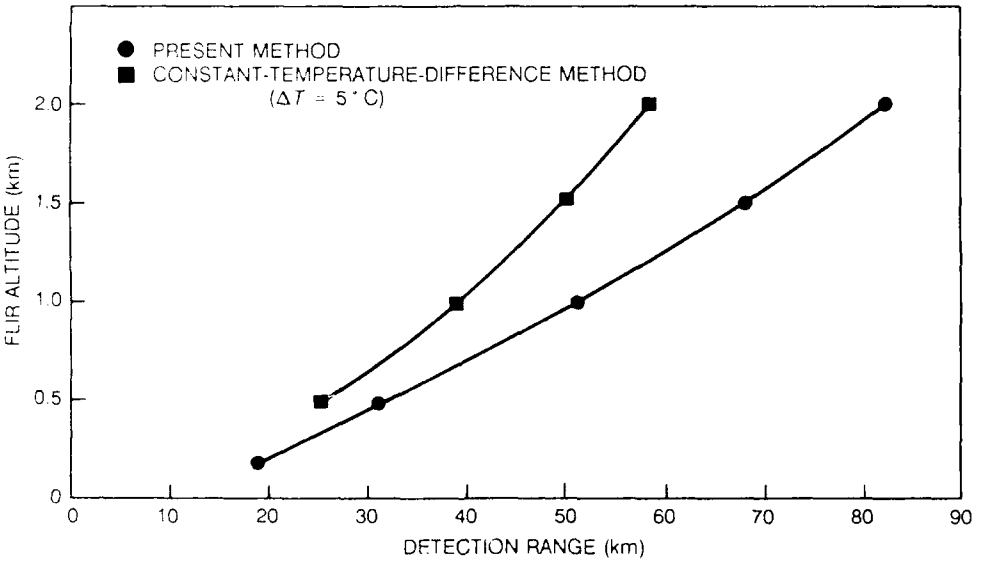

Figure 28. Comparison of the MDRs (lower envelope) for the USS *Brooke* (FFG1) calculated with the current algorithm and with the method that assumes a constant temperature difference of 5°C between the ship and its background.

CONCLUSIONS AND RECOMMENDATIONS

In the absence of transmission or radiometric measurements, the LOWTRAN codes must currently be relied on, along with measured meteorological parameters and models of aerosol size distributions, to predict the atmospheric effects on EO system performance. These codes have proven to be a versatile tool in predicting atmospheric radiance. NAM has undergone considerable evaluation and should be considered a workable model in performance predictions. While NOVAM is still in the development and validation stage, it shows promise of accounting for the dynamic changes within the mixed layer and should transition into LOWTRAN in the near future. Still lacking is the ability to measure the air mass factors and slant-path visibility in operational conditions. Emphasis should be placed on alternative methods, such as the sky radiance technique, rather than on air mass characterization for determining the required input parameters.

While the remote-sensing potential of lidars shows promise, the capability of deriving extinction coefficients from backscatter measurements has not been demonstrated with any assured degree of accuracy when the atmosphere is inhomogeneous. The two-angle technique certainly would be useful in situations where the atmosphere can be shown to be horizontally homogeneous, provided that the system calibration can be accurately determined. The double-ended technique resolves the requirement for knowing the relationship between backscatter and extinction. However, the requirement for having an instrumented range at both ends is impractical in an operational situation. It appears that the double-ended technique is best suited for aerosol studies and model validation.

The reliability of the sea surface radiance model that uses the LOWTRAN 6 NAM to accurately represent measured values for low wind and moderate wind speed conditions has been demonstrated. Whether or not it will be representative of other wind speed conditions needs to be determined. Also, the preliminary evaluation of the average ship temperature model showed promise, since this model responds to the differing solar conditions. Future attempts at validation must ensure the accuracy of the ambient meteorological conditions. Onboard ground-truth radiometry measurements of the temperatures of different portions of the ship are also needed to aid in determining the accuracy of the adjusted average temperatures inferred from the AGA measurements. Finally, a controlled experiment with an airborne operational system must be conducted to determine the validity of the predicted detection ranges under varying meteorological conditions.

REFERENCES

Batley, P.E., "Ship Infrared Signatures (SIRS) Computer Model Technical Overview and User's Manual," David Taylor Naval Ship Research and Development Center Report SME-78-37 (1978).

Bissonnette, L.R., "Sensitivity Analysis of Lidar Inversion Algorithms," Appl. Opt., *25*, 2122 (1985).

Burns, R.H. et al., "Description of the Ship Infrared Electro-Optical Scenario (SIREOS) Computer Model, David Taylor Naval Ship Research and Development Center Report 80 097 (1980).

Cox, C., and W. Munk, "Measurements of Roughness of the Sea Surface from Photographs of the Sun's Glitter," Jour. Opt. Soc. of Am., *44*, 838 (1954).

de Leeuw, G., "Vertical Profiles of Giant Particles Close Above the Sea Surface," TELLUS, *38B*, 51 (1986).

de Leeuw, G., G.J. Kunz, and C.W. Lamberts, "Humidity Effects on the Backscatter Extinction Ratio," Appl. Opt., *25*, 3971 (1986).

de Leeuw, G., K.L. Davidson, S.G. Gathman, and R.V. Noonkester, "Physical Models for Aerosol in the Marine Mixed-Layer," Conference Proceedings of the 44th AGARD Symposium of the Electromagnetic Wave Propagation Panel on "Operational Decision Aids for Exploiting or Mitigating Electromagnetic Propagation Effects," CP453, Paper No. 40 (1989).

Ferguson, J.A., and D.H. Stephens, "Algorithm for Inverting Lidar Returns," Appl. Opt., *24*, 3673 (1983).

Fitzgerald, J.W., "Approximate Formulas for the Equilibrium Size of an Aerosol Particle as a Function of its Dry Size and Composition and the Ambient Relative Humidity," J. Appl. Meteorol., *14*, 1044 (1975).

Fitzgerald, J.W., "Effect of Relative Humidity on the Aerosol Backscattering Coefficient at .694-and-10.6 μm Wavelengths," Appl. Opt. *23*, 411 (1984).

Gathman, S.G., "Optical Properties of the Marine Aerosol as Predicted by the Navy Aerosol Model," Opt. Eng., *22*, 57 (1983).

Gathman, S.G., "A Preliminary Description of NOVAM, the Navy Oceanic Vertical Aerosol Model," Naval Research Laboratory Technical Report 9200 (1989).

Gathman, S.G., and B. Ulfers, "On the Accuracy of IR Predictions Made by the Navy Aerosol Model," American Meteorology Society Ninth Conf. on Aerospace and Aeronautical Meteorology, pp. 194 198 (1983).

Griggs, M., "Measurements of Atmospheric Aerosol Thickness using ERTS-1 Data," Jour. Air Pollut. Control Assoc., *25*, 622 (1975).

Hughes, H.G., "Evaluation of the LOWTRAN 6 Navy Maritime Aerosol Model Using 8 to 12 μm Sky Radiances," Opt. Eng., *26*, 1155 (1987).

Hughes, H.G., "Apparent Infrared Radiance of the Sea," Naval Ocean Systems Center, TR-1271 (1989a).

Hughes, H.G., "Sea and Sky Infrared Radiances Near the Horizon," Naval Ocean Systems Center, TR-1294 (1989b).

Hughes, H.G., "Airborne FLIR Detection of Surface Targets," Naval Ocean Systems Center, TR-1275 (1989c).

Hughes, H.G., and D.R. Jensen, "Aerosol Model Selection Using Surface Measurements of IR Horizon Radiances and Satellite Detected Visible Radiances," Appl. Opt., *27*, 4367 (1988).

Hughes, H.G., and M.R. Paulson, "Double-Ended Lidar Technique for Aerosol Studies," Appl. Opt., *27*, 2273 (1988).

Hughes, H.G., and J.H. Richter, "Extinction Coefficients Calculated from Aerosol Size Distributions Measured in a Marine Environment," Proceedings of the Society of Photo-Optical Instrumentation Engineers (SPIE), San Diego, California, Volume 195, pp 39-45 (1979).

Klett, J.D., "Lidar Inversion with Variable Backscatter/Extinction Ratios," Appl. Opt., *11*, 1638 (1985).

Kneizys, F.X., E.P. Shettle, W.O. Gallery, J.H. Chetwynd, Jr., J.H. Abreu, J.E.A. Selby, S.A. Clough, and R.W. Fenn, "Atmospheric Transmittance/Radiance: Computer Code LOWTRAN 6, Air Force Geophysical Laboratory Technical Report No. 83-0187 (1983).

Kneizys, F.X., E.P. Shettle, L.W. Abreu, J.H. Chetwynd, Jr., G.P. Anderson, W.O. Gallery, J.E.A. Selby, and S.A. Clough, "Users Guide to LOWTRAN 7, AFGL-TR-88-0177 (1988).

Kunz, G.J., "Bipath Method as a Way to Measure the Spatial Backscatter and Extinction Coefficients with Lidar," Appl. Opt., *26*, 794 (1987).

Kunz, G.J., "A Method for Measuring the Vertical Extinction and Backscatter Profile with a Scanning Lidar," TNO Physics and Electronics Laboratory, Report No. FEL 1988-65 (1988).

Lindberg, J.D., W.J. Lentz, E.M. Measure, and R. Rubio, "Lidar Determination of Extinction in Stratus Clouds," Appl. Opt., *23*, 2172 (1984).

Miller, W.B., and J.C. Ricklin, "A Module for Imaging Through Optical Turbulence (IMTURB)," US Army Atmospheric Sciences Laboratory, Report No. ASL-TR-0221-27 (1987).

Mulders, J.M., "Algorithm for Inverting Lidar Returns: Comment," Appl. Opt., *23*, 2855 (1984).

Ostrowski, P.P., and D.M. Wilson, "A Simplified Computer Code for Predicting Ship Infrared Signatures," Naval Surface Weapons Center TR 84-540 (1985).

Paulson, M.R., "Evaluation of a Dual-Lidar Method for Measuring Aerosol Extinction," Naval Ocean Systems Center, TD-1075 (1987).

Paulson, M.R., Atmospheric Horizontal-Inhomogeneity Effects on the Optical Depths Determined by the Double-Elevation-Angle Lidar Technique," Naval Ocean Systems Center, TD-1600 (1989).

Russell, P.B., and J.M. Livingston, "Slant-Path Extinction Measurements and Their Relation to Measured and Calculated Albedo Changes," J. Clim. and Appl. Meteor. *23*, 1204 (1984).

Salemink, H.W.M., P. Schotanus, and J.B. Bergwerff, "Quantitative Lidar at 532 nm for Vertical Extinction Profiles and the Effect of Relative Humidity," Appl. Phys., B34, 187 (1984).

Selby, J.A.F E.P. Shettle, and R.A. McClatchey, "Atmospheric Transmittance from 0.25 to 28.5 μm: Supplement LOWTRAN 3B (1976)," AFGL-TR-76-0258 (1976).

Wollenweber, F.G., "Effects of Atmospheric Model Layering on LOWTRAN 6 Calculations of 8 to 12 μm Near Horizon Sky Radiances," Naval Ocean Systems Center TD 1193 (1988a).

Wollenweber, F.G., "Infrared Sea Radiance Modeling Using LOWTRAN 6," Naval Ocean Systems Center TD 1355 (1988b).